PERGAMON

International Journal of Solids and Structures 38 (2001) 605–633

INTERNATIONAL JOURNAL OF SOLIDS and STRUCTURES

www.elsevier.com/locate/ijsolstr

Finite element analysis of piezoceramic components taking into account ferroelectric hysteresis behavior

Marc Kamlah *,[1], Ulrich Böhle

Forschungszentrum Karlsruhe, Institut für Materialforschung II, Technik und Umwelt, Postfach 3640, D-76021 Karlsruhe, Germany

Received 1 May 1999; in revised form 11 February 2000

Abstract

A simplifying macroscopic constitutive law for ferroelectric and ferroelastic hysteresis effects of piezoceramics is presented. After summarizing the uniaxial formulation motivated elsewhere (Kamlah, M., Tsakmakis, C., 1999. Int. J. Solids Struct. 36, 669–695; Kamlah, M., Böhle, U., Munz, D., Tsakmakis, Ch., 1997. Smart Structures and Materials 1997: Mathematics and Control in Smart Structures, Proceedings of SPIE, vol. 3039, 144–155), it is generalized to a three-dimensional tensorial formulation. The model has been implemented in the public domain finite element code PSU of Stuttgart University. The finite element analysis is carried out in a two-step scheme: First the purely dielectric boundary value problem is solved for the history of the electric potential. Second, prescribing this electric potential, the electro-mechanical stress analysis for the mechanical boundary conditions yields the electro-mechanical fields as, for instance, the mechanical stress field. In order to verify the capabilities of our tool, a multilayer-like actuator geometry is analyzed. It is shown that the remanent polarization remaining after poling gives rise to a non-vanishing distribution of the electric potential even it is reduced to zero at the electrodes. Concerning the residual stresses present after poling, a tensile stress field perpendicular to the direction of the electrodes can be found in the passive region of the actuator where so-called poling cracks are known to occur. It is concluded that our finite element tool is suitable for studying the influence of geometry and material parameters on the stresses in critical regions of piezoceramic devices.

Keywords: Piezoceramic; Ferroelectric hysteresis; Ferroelastic hysteresis; Constitutive law; Finite element; Stress analysis

1. Introduction

1.1. State of the art

For precisely controlled actuation applications with extremely short rise times, piezoceramic actuators are the number one choice. A typical example is the reduction of harmful exhaust of combustion engines by

* Corresponding author. Fax: +49-7247-822347.
E-mail address: marc.kamlah@imf.fzk.de (M. Kamlah).
[1] http://www.fzk.de/izsm/

0020-7683/01/$ - see front matter
PII: S0020-7683(00)00055-X

injecting the fuel during each operation cycle according to an exactly prescribed time strategy. Currently, there are strong efforts in the industry, to realize this by means of multilayered stack acuators (for the working principle of multilayered actuators see e.g. Bowen et al. (1980) and Uchino (1993). One of the key problems is to meet the rigorous request for reliability which means, for example, in the car industry a lifetime of more than 5×10^8 cycles at a failure rate of less than 10^{-5}.

In order to assess the reliability of a component, one has to know, as precisely as possible, the mechanical stress state which in turn depends strongly on the constitutive properties of the material in question. Because of their outstanding electro-mechanical coupling properties, lead zirconate titanate (PZT) ceramics are widely used to exploit the piezoelectric effect (Newnham, 1989; Cross, 1993, 1995). However, besides reversible piezoelectric behavior, these materials exhibit due to domain switching processes significant irreversible ferroelectric and ferroelastic hysteresis properties if loaded by electric or mechanical loads of sufficient magnitude. (For basic properties of PZT, see the standard literature, e.g. Fatuzzo and Merz (1967), Jaffe et al. (1971), Feldtkeller (1973) and Lines and Glass (1977). For recent experimental investigations of the macroscopic phenomena induced by microscopic domain switching see Cao and Evans (1993), Schäufele and Härdtl (1996) and Lynch (1996).

As long as loadings are small enough, the response behavior of piezoceramics can be approximated by the well-established classical linear piezoelectric theory. This theory has been solved analytically for many problems and can also be found implemented in commercial finite element codes. (For a not- at-all representative selection of applications of this theory in linear piezoelectric fracture mechanics see Parton and Kudryavtsev (1988), McMeeking (1989), Pak (1992), Suo et al. (1992), Sosa (1992), Dunn (1994), Kumar and Singh (1996), Kuna (1998) and Balke et al. (1998) However, the restriction to small signal behavior is no longer justified in general for, nowadays, applications involving complicated geometries and severe loadings. Obviously, for a representative stress analysis, the so-called large signal hysteresis behavior has to be taken into account.

Thus, the following problem is posed: The equilibrium condition and the Gaussian law have to be solved in conjunction with an appropriate constitutive law relating on a macroscopic level stress and polarization to the histories of strain and electric field. Even though work on the non-linear constitutive modeling of piezoceramics is still rare, there has been increasing activity on this field in the past years. Very unlike the traditional area of non-linear mechanical behavior of structural materials, microscopically motivated approaches to describing the constitutive behavior of piezoceramics are dominating (Hwang et al., 1995; Huo and Jiang, 1997; Chen et al., 1997; Chen and Lynch, 1998; Michelitsch and Kreher, 1998; Steinkopff, 1999; Hwang and McMeeking, 1998, 1999; Huber et al., 1998). Based on a more or less sound micro-physical foundation, these approaches allow one typically to simulate macroscopic phenomena, like dielectric or butterfly hysteresis, however, lacking computational efficiency at the same time. Furthermore, these models are usually closely connected to a purely tetragonal symmetry on the microscopic scale. (Commercial PZT ceramics are preferably in a phase state close to the so-called morphotropic phase boundary where tetragonal as well as rhombohedral phase fractions are present. (Jaffe et al., 1971); for a recent review see Cross (1998). Meanwhile, Chen and Lynch (1999) have developed a non-linear finite element method based on their micro-electro-mechanical model. Switching processes in a rectangular plate with an elliptic hole under electric loadings are analyzed.

A purely phenomenological approach has first been applied by Chen and coworkers (e.g. Chen and Peercy, 1979; Chen and Montgomery, 1980; Chen and Marsden, 1981; Chen, 1980) followed by the work of Bassiouny et al. (1988) and Bassiouny and Maugin (1989) (cf. Chapter 6 in Maugin et al., 1992). However, we are not aware of any scientific work attempting to develop these approaches further to a status ready for application in engineering reliability analyses. In a certain sense, this appears to be surprising, since in engineering one usually deals with macroscopic structures where the macroscopic constitutive behavior can be described probably most efficiently by phenomenological methods. Ghandi and Hagood (1997) motivated a model relying essentially on an energy function employing non-linear higher order terms and

developed a corresponding finite element tool. However, the model is very sensible to changes of the higher order coefficients which are difficult to determine and it includes no ferroelasticity.

In view of this situation, the work of Kamlah and Tsakmakis (1999), extended by Kamlah et al. (1997), constructed by phenomenological methods a simple model for the ferroelectric and ferroelastic behavior of PZT ceramics (see also Kamlah et al., 1998). In these papers, the model was restricted to uniaxial electromechanical loadings. Meanwhile, a three-dimensional formulation of the model is available, which will be presented in this paper (for a recent phenomenological model see also Fan et al. (1999) and Lynch (1998)). We want to emphasize that application of phenomenological methods is by no means an excuse for physical arbitraryness. Rather, we consider the construction of a valid phenomenological model for piezoceramics as possible only if it is strictly motivated by findings about microscopic domain processes. Of course, another important cornerstone is given by experiments on macroscopic specimens of bulk material. Information about loading conditions not available in experiments, for instance homogeneous three-dimensional loadings, may be provided by numerical simulations with the help of microscopically based models like those mentioned above (see the corresponding statement of Hwang and McMeeking (1999)).

We adopt the classical approach of structural engineering, first to formulate mathematically a complete theory for the large signal behavior of piezoceramics in terms of partial differential equations for the balance laws and ordinary differential equations for the constitutive law. Then, in the second step, an appropriate numerical solution method for the resulting boundary value problems, in structural engineering usually the finite element method, has to be chosen, since in general an analytical solution will hardly be possible. This approach has already been applied successfully to the coupled electro-mechanical behavior of electrostrictive materials (Suo, 1991; Yang and Suo, 1994; Hom and Shankar, 1994, 1995, 1996; Gong, 1995; Gong and Suo, 1996). As a substantial simplification compared to our problem, the restriction to electrostrictive behavior allows one to neglect memory effects in the material response. From our point of view, no numerical methods or computer algorithms or particular software codes should be part of the formulation of the theory. They should not enter the picture before solution tools for the mathematical formulation of the theory are needed. (This is, at least partly, in contrast to some of the approaches found in the literature like several of the microscopic models mentioned above.)

1.2. Scope and plan of the paper

It is the scope of this paper, to give a first hand idea of the importance of ferroelectric and ferroelastic hysteresis phenomena for the state of components made of piezoceramics. A very important aspect is the residual stress state due to poling after sintering. These very first experiences can be gained in a most transparent way by means of a constitutive model as simple as possible, allowing to study the behavior of a structure under the influence of a very few, but typical parameters. In the case of piezoceramics, besides the classical small signal parameters, coercive field, maximum remanent polarization, coercive stress, and maximum remanent strain are such parameters.

In view of this guide line, the present paper is organized as follows: In Section 2, we present a simple constitutive law for the non-linearly coupled ferroelectric and ferroelastic hysteresis behavior of piezoceramics. It relies on the introduction of remanent polarization and remanent strain as phenomenological internal variables besides stress, strain, electric field and polarization. The internal variables are governed by ordinary differential equations and each of these evolution equations is subjected to two loading conditions of different nature. The first one indicates the onset of changes of the remanent quantities by domain switching, while the second one characterizes the saturation value of a remanent quantity corresponding to a totally switched domain structure. Polarization-induced anisotropy in the piezoelectricity tensor is taken into account; however, for simplicity, no rate effects are included. By means of a bilinear approximation, the following characteristic phenomena of piezoceramics are represented: dielectric hysteresis, polarization induced piezoelectricity, butterfly hysteresis, ferroelastic hysteresis, mechanical depolarization, field

dependent coercive stress. After summarizing the uniaxial formulation of the evolution laws given before (Kamlah and Tsakmakis, 1999; Kamlah et al., 1997), we present a three-dimensional generalization of the model.

In Section 3, the current state of the finite element implementation of the model is described. The electromechanical stress analysis is carried out in a two-step procedure well established for thermomechanical structure analyses. In the first step, the purely dielectric boundary value problem for the body under consideration is solved, yielding the history of the field of the electric potential. In the second step, this electric potential as well as the mechanical boundary conditions are prescribed, giving the electromechanical solution of the histories of stress, strain, polarization, electric field and the internal variables. Obviously, this electro-mechanical stress analysis does not yield the fully coupled solution, since the mechanical boundary conditions have no influence on the solution for the electric potential. However, it is expected, that the influence of the mechanical boundary conditions on the dielectric solution is much weaker then the other way around (cf. Gong, 1995).

In Section 4, we demonstrate the potential of our finite element tool by an electro-mechanical stress analysis of the poling process of a simplified multilayer actuator geometry. In order to reduce computational expenditure, symmetry assumptions are exploited and therefore the actuator is represented by a plane strain finite element model consisting of a single PZT layer between two electrodes. The model represents the typical alternating electrode arrangement of nowadays multilayer actuator designs. It turns out that the solution is significantly dominated by some basic features of the underlying ferroelectric constitutive law. As can be expected, a remanent polarization is present after the poling electric potential has been brought back to zero values at the electrodes. Since the fully poled state yields a remanent polarization which is not divergence-free, it gives rise to a significant non-zero distribution of the electric potential within the poled ceramic, even though it is zero at the electrodes. The stress analysis is carried out by means of a plane strain formulation. The resulting residual stress state in the structure is clearly influenced by the existence of ferroelectric and ferroelastic hysteresis properties. In particular, after poling, significant tensile stresses normal to the electrode are found in front of the tip of the electrode, exactly where the so-called poling cracks are known to occur.

In the following analysis which is restricted to a geometrically linear setting, all component representations of tensors are referred to a Cartesian coordinate system (summation convention). First-order tensors (*vectors*) are denoted by upright letters with superscript arrows ($\vec{\mathrm{a}}$, $\vec{\mathrm{A}}$) and second-order tensors (*tensors*) by bold slanted letters ($\boldsymbol{a}$, $\boldsymbol{A}$, $\boldsymbol{\alpha}$). A dot between tensors indicates the contraction relative to one index, for example, the inner product between vectors, i.e. $\vec{\mathrm{a}} \cdot \vec{\mathrm{b}} = \mathrm{a}_i \mathrm{b}_i$, the composition of two tensors, i.e. $\boldsymbol{A} \cdot \boldsymbol{A}^{-1} = \boldsymbol{I}$ ($\boldsymbol{A}^{-1}$: inverse of $\boldsymbol{A}$, $\boldsymbol{I}$: identity tensor), the inner product between tensors, i.e. $\boldsymbol{A} : \boldsymbol{B} = \mathrm{tr}(\boldsymbol{A} \cdot \boldsymbol{B}^{\mathrm{T}}) = A_{ij} B_{ij}$ ($\mathrm{tr}\,\boldsymbol{A}$: trace of $\boldsymbol{A}$. $\boldsymbol{B}^{\mathrm{T}}$: transpose of $\boldsymbol{B}$), the linear mapping of a vector by a tensor, i.e. $\boldsymbol{A} \cdot \vec{\mathrm{a}} = A_{ij} \mathrm{a}_j$. $\boldsymbol{A}^D = \boldsymbol{A} - 1/3(\mathrm{tr}\,\boldsymbol{A})\boldsymbol{I}$ stands for the deviator of $\boldsymbol{A}$ and $\|\boldsymbol{A}\| = \sqrt{\boldsymbol{A} : \boldsymbol{A}}$ is the norm of the tensor $\boldsymbol{A}$. $\vec{\mathrm{e}}_{\mathrm{a}} = \vec{\mathrm{a}}/\|\vec{\mathrm{a}}\|$ is the unit vector in the direction of the vector $\vec{\mathrm{a}}$ ($\|\vec{\mathrm{a}}\| = \sqrt{\vec{\mathrm{a}} \cdot \vec{\mathrm{a}}}$: norm of $\vec{\mathrm{a}}$). The symbol $\otimes$ indicates the dyadic product, e.g. $\vec{\mathrm{a}} \otimes \vec{\mathrm{b}}$ yields a second-order tensor with components $\mathrm{a}_i \mathrm{b}_j$. $(\dot{\ }) = \mathrm{d}(\ )/\mathrm{d}t$ denotes the time derivative of a field ( ). Further mathematical definitions will be given where they are needed.

2. A simple constitutive model for ferroelectric and ferroelastic piezoceramics

For a macroscopic theory of a deformable dielectric, a relation for the dependence of the *electric field* $\vec{E} = -\mathrm{grad}\,\varphi$ and the *stress tensor* $\boldsymbol{T}$ on the histories of the polarization $\vec{P}$ and the *strain tensor* $\boldsymbol{S} = 1/2(\mathrm{grad}\,\vec{\mathrm{u}} + (\mathrm{grad}\,\vec{\mathrm{u}})^{\mathrm{T}})$ is needed ($\varphi, \vec{\mathrm{u}}$: *electric potential* and *displacement vector*, respectively). In Sections 2.1 and 2.2, we first summarize our proposal for such a constitutive model, as it has been moti-

vated in full detail for uniaxial electro-mechanical loadings in Kamlah and Tsakmakis (1999) and Kamlah et al. (1997). Then, the evolution laws are generalized to a three-dimensional tensorial formulation.

2.1. The general structure of the model

The basic assumption of our model is to introduce the *irreversible* or *remanent polarization* $\vec{P}^{i}$ and the *irreversible* or *remanent strain* $\boldsymbol{S}^{i}$ as internal variables by the additive decompositions

$$\vec{P} = \vec{P}^{r} + \vec{P}^{i}, \tag{1}$$

$$\boldsymbol{S} = \boldsymbol{S}^{r} + \boldsymbol{S}^{i} \tag{2}$$

of the polarization and the strain, respectively (see also Bassiouny et al., 1988). The macroscopic internal variables $\vec{P}^{i}$ and $\boldsymbol{S}^{i}$ must be understood as averages of the corresponding microscopic quantities, i.e. the spontaneous polarization and the spontaneous strain of a domain. Please note that the notion of irreversibility is introduced here as a synonym of remanence and without explicit reference to a thermodynamic framework.

The parts $\vec{P}^{r}$ and $\boldsymbol{S}^{r}$ are assumed to be *reversible* in the sense that they vanish if the loads $\vec{E}$ and $\boldsymbol{T}$ are zero. As a simple choice, we adopt for them equations of linear piezoelectric structure:

$$\vec{P}^{r} = \mathbb{d} : \boldsymbol{T} + \boldsymbol{\epsilon} \cdot \vec{E}, \tag{3}$$

$$\boldsymbol{S}^{r} = \mathbb{C}^{-1} : \boldsymbol{T} + \mathbb{d}^{T} \cdot \vec{E}. \tag{4}$$

$\boldsymbol{\epsilon}$, $\mathbb{d}$, and $\mathbb{C}$ are the (second order) *tensor of dielectric permittivities*, the (third order) *tensor of piezoelectric moduli*, and the (fourth order) *tensor of elastic moduli*, respectively. In order to keep the model as simple as possible, we neglect the influence of the loading history on the anisotropy of $\boldsymbol{\epsilon}$ and $\mathbb{C}$ and assume isotropic representations, where ϵ, μ, and ν are the *dielectric constant*, *shear modulus*, and *Poisson ratio*, respectively ($\boldsymbol{I}, \mathbb{I}$: identity tensors of second and fourth order, respectively):

$$\boldsymbol{\epsilon} = \epsilon \boldsymbol{I}, \qquad \mathbb{C} = 2\mu\left(\mathbb{I} + \frac{\nu}{1-2\nu}\boldsymbol{I} \otimes \boldsymbol{I}\right). \tag{5a,b}$$

Note, that this restriction is not essential for our approach (for similar assumptions see Hwang et al. (1995) and related papers).

The situation is completely different for the piezoelectricity tensor. The history dependence of the anisotropy cannot be neglected here, since the piezoelectric properties are not just modified as is the case with dielectricity and elasticity. Rather, the phenomenon of macroscopic piezoelectricity is absent in the unpoled state, i.e., if there is no macroscopic remanent polarization $\vec{P}^{i}$. Furthermore, in the fully poled state, we have transversely isotropic piezoelectricity, where the axis of anisotropy coincides with the direction $\vec{e}_{P^i}$ of poling. Therefore, we assume the representation

$$d_{kij}(\vec{P}^{i}) = \frac{\left\|\vec{P}^{i}\right\|}{P_{sat}}\left\{d_{\|}e_i e_j e_k + d_{\perp}(\delta_{ij} - e_i e_j)e_k + d_{=\frac{1}{2}}\left[\left((\delta_{ki} - e_k e_i)e_j + (\delta_{kj} - e_k e_j)e_i\right)\right]\right\} \tag{6}$$

for the piezoelectricity tensor, where the constants $d_{\|}, d_{\perp}, d_{=}$ correspond to the well-known parameters d_{33}, d_{31}, d_{15}, respectively, and P_{sat} is the *maximum remanent polarization* ($d_{kij} = (\mathbb{d})_{kij}, e_i = (\vec{e}_{P^i})_i$ is the ith component of $\vec{e}_{P^i}$).

The macroscopic remanent polarization $\vec{P}^{i}$ stands for the net polarization of a neighborhood of many polarized domains with possibly different orientations and is a measure of the extent of alignment of the domains in a certain direction. The change of alignment of the domains causes a change of the remanent

strain of this neighbourhood and it may be represented as uniaxial strain state in the direction of $\vec{P}^{i}$. Thus, we relate the remanent polarization $\vec{P}^{i}$ to the part

$$\boldsymbol{S}^{p} = \frac{3}{2} S_{sat} \frac{\left\|\vec{P}^{i}\right\|}{P_{sat}} \left(\vec{e}_{P^{i}} \otimes \vec{e}_{P^{i}} - \frac{1}{3} \boldsymbol{I} \right) \tag{7}$$

of the remanent strain (S_{sat} is the *maximum remanent polarization*). Since experimental findings indicate that changes of the macroscopic strain state due to domain switching are volume preserving, we constructed $\boldsymbol{S}^{p}$ such that it yields a deviatoric uniaxial strain state in the direction of $\vec{P}^{i}$ (cf. Cao and Evans, 1993). The strain tensor (7) yields a normal strain of $S_{sat}\left\|\vec{P}^{i}\right\|/P_{sat}$ in the direction of poling and a transverse strain of $-1/2 S_{sat}\left\|\vec{P}^{i}\right\|/P_{sat}$ perpendicular to it. This is the structure assumed usually for the remanent strain induced by the remanent polarization (cf. Hwang et al., 1995; Huo and Jiang, 1997).

Domain switching can also be induced by mechanical stresses. In the case of an initially unpoled material, the state of macroscopic polarization remains unchanged, while purely ferroelastic irreversible strain changes occur. Therefore, we also have to consider a ferroelastic contribution $\boldsymbol{S}^{f}$ to the remanent strain, the latter consisting in the general case of a superposition of both parts:

$$\boldsymbol{S}^{i} = \boldsymbol{S}^{p} + \boldsymbol{S}^{f}. \tag{8}$$

The general structure of the constitutive law is shown below. The system of equations has to be closed by evolution equations for $\vec{P}^{i}$ and $\boldsymbol{S}^{f}$. See principle procedure for the construction of the evolution laws in Section 2.3.

- additive decomposition

$$\vec{P} = \vec{P}^{r} + \vec{P}^{i},$$

$$\boldsymbol{S} = \boldsymbol{S}^{r} + \boldsymbol{S}^{i},$$

- representation of reversible behavior

$$\vec{P}^{r} = \mathbb{d} : \boldsymbol{T} + \boldsymbol{\epsilon} \cdot \vec{E},$$

$$\boldsymbol{S}^{r} = \mathbb{C}^{-1} : \boldsymbol{T} + \mathbb{d}^{T} \cdot \vec{E},$$

  - isotropic dielectricity and elasticity

$$\boldsymbol{\epsilon} = \epsilon \boldsymbol{I}, \quad \mathbb{C} = 2\mu\left(\mathbb{I} + \frac{v}{1-2v} \boldsymbol{I} \otimes \boldsymbol{I} \right),$$

  - transversally isotropic piezoelectricity

$$d_{kij}(\vec{P}^{i}) = \frac{\left\|\vec{P}^{i}\right\|}{P_{sat}} \left\{ d_{\|} e_i e_j e_k + d_{\perp}(\delta_{ij} - e_i e_j) e_k + d_{=\frac{1}{2}} \left[\left((\delta_{ki} - e_k e_i) e_j + (\delta_{kj} - e_k e_j) e_i \right) \right] \right\},$$

- remanent strain

$$\boldsymbol{S}^{i} = \frac{3}{2} S_{sat} \frac{\left\|\vec{P}^{i}\right\|}{P_{sat}} \left(\vec{e}_{P^{i}} \otimes \vec{e}_{P^{i}} - \frac{1}{3} \boldsymbol{I} \right) + \boldsymbol{S}^{f}.$$

Since according to Eq. (7), $\boldsymbol{S}^{p}$ is simply a function of $\vec{P}^{i}$, the constitutive law has to be completed by evolution laws for the remanent polarization $\vec{P}^{i}$ and for the ferroelastic part $\boldsymbol{S}^{f}$ of the remanent strain, the latter allowing for deviatoric ferroelastic strain changes only. From the formulation of these evolution equations, it will be clear that Eq. (8) does not imply that the influence of electric and mechanical loads on

$\boldsymbol{S}^{\mathrm{i}}$ can be decomposed additively (cf. Kamlah and Tsakmakis, 1999). As a first step towards the formulation of evolution equations describing the history dependence of the material adequately, we consider uniaxial electro-mechanical loadings next.

2.2. Uniaxial electro-mechanical loadings

Let us denote the components of $\vec{\mathrm{E}}, \vec{\mathrm{P}}, \vec{\mathrm{P}}^{\mathrm{i}}, \boldsymbol{T}, \boldsymbol{S}, \boldsymbol{S}^{\mathrm{i}}, \boldsymbol{S}^{\mathrm{p}}, \boldsymbol{S}^{\mathrm{f}}$ in the direction of the loading (e. g. the x_3-direction) by $E, P, P^{\mathrm{i}}, \sigma, S, S^{\mathrm{i}}, S^{\mathrm{p}}, S^{\mathrm{f}}$, respectively. Then, the additive decompositions (1) and (2) reads

$$P = P^{\mathrm{r}} + P^{\mathrm{i}}, \tag{9}$$

$$S = S^{\mathrm{r}} + S^{\mathrm{i}}, \tag{10}$$

where according to Eqs. (8) and (7)

$$S^{\mathrm{i}} = S^{\mathrm{f}} + S^{\mathrm{p}} = S^{\mathrm{f}} + S_{\mathrm{sat}} \frac{|P^{\mathrm{i}}|}{P_{\mathrm{sat}}}. \tag{11}$$

From Eqs. (3)–(6) one finds that the reversible parts of P and S are related to the electric field E and the uniaxial stress σ by

$$P^{\mathrm{r}} = d \frac{P^{\mathrm{i}}}{P_{\mathrm{sat}}} \sigma + \epsilon E, \tag{12}$$

$$S^{\mathrm{r}} = \frac{1}{Y} \sigma + d \frac{P^{\mathrm{i}}}{P_{\mathrm{sat}}} E, \tag{13}$$

where $Y = 2\mu(1+\nu)$ is *Young's modulus* and $d := d_{\parallel}$. Note the history dependence of the piezoelectric coefficient via the internal variable P^{i}.

The basis for the construction of evolution equations for the internal variables P^{i} and S^{f} is given by a total of four criteria, indicating different critical and saturation states. The principle idea is as follows: Two criteria, $f^{\mathrm{p}} = 0$ and $f^{\mathrm{f}} = 0$, indicate the onset of domain switching, being induced either electrically ($|E| = E_{\mathrm{c}}$) or mechanically ($|\sigma| = \sigma_{\mathrm{c}}$), respectively ($E_{\mathrm{c}}, \sigma_{\mathrm{c}}$: *coercive field* and *coercive stress*, respectively). Two further criteria, $h^{\mathrm{p}} = 0$ and $h^{\mathrm{f}} = 0$, indicate the saturation of remanent polarization ($|P^{\mathrm{i}}| = P_{\mathrm{sat}}$) and strain ($|S^{\mathrm{i}}| = S_{\mathrm{sat}}$), respectively, belonging to a fully switched domain structure. From these criteria, the evolution equations are derived by exploiting the so-called consistency condition, thereby leading to rate-independent laws.

Let us consider the evolution law of P^{i} first. For the motivation of the equations summarized in the following, we refer the reader to Kamlah and Tsakmakis (1999) and Kamlah et al. (1997), once more. We assume the existence of a range of reversible behavior in the sense that for values of the electric field inside this range, the irreversible polarization does not change:

$$f^{\mathrm{p}}(E, P^{\mathrm{i}}) = |E - c^{\mathrm{p}} P^{\mathrm{i}}| - E_{\mathrm{c}}. \tag{14}$$

E_{c} is the coercive field and c^{p} is a non-negative constant. On the other hand, the saturated state for the remanent polarization is indicated by

$$h^{\mathrm{p}} = |P^{\mathrm{i}}| - \hat{P}_{\mathrm{sat}}(\sigma, E, P^{\mathrm{i}}), \tag{15}$$

where, in general, the saturation value for the irreversible polarization may depend on the loading history via $\sigma, E, P^{\mathrm{i}}$. Then, the evolution law for P^{i} can be formulated as

$$\dot{\mathrm{P}}^{\mathrm{i}} = \begin{cases} \lambda_h^{\mathrm{p}} \frac{\partial h^{\mathrm{p}}}{\partial P^{\mathrm{i}}} & \text{if } \ h^{\mathrm{p}} = 0 \text{ and loading,} \\ \lambda_f^{\mathrm{p}} \frac{\partial f^{\mathrm{p}}}{\partial E} & \text{else if } \ f^{\mathrm{p}} = 0 \text{ and loading,} \\ 0 & \text{else.} \end{cases} \tag{16}$$

The factors of proportionality λ_h^{p} and λ_f^{p} have to be determined by the consistency conditions $(\mathrm{d}h^{\mathrm{p}}/\mathrm{d}t) = 0$ and $(\mathrm{d}f^{\mathrm{p}}/\mathrm{d}t) = 0$, respectively. For a precise mathematical formulation of the loading conditions, we introduce the notations

$$\lfloor x \rceil = \begin{cases} 1, & x \geqslant 0, \\ 0, & x < 0, \end{cases} \qquad \lceil x \rfloor = \begin{cases} 1, & x > 0 \\ 0, & x \leqslant 0, \end{cases} \tag{17}$$

and

$$\overset{*}{f}{}^{\mathrm{p}} = \frac{\mathrm{d}}{\mathrm{d}t} f^{\mathrm{p}} \bigg|_{\dot{\mathrm{P}}^{\mathrm{i}}=0,}, \qquad \overset{*}{h}{}^{\mathrm{p}} = \frac{\mathrm{d}}{\mathrm{d}t} h^{\mathrm{p}} \bigg|_{\dot{\mathrm{P}}^{\mathrm{i}} = \lfloor f^{\mathrm{p}} \rceil \lfloor \overset{*}{f}{}^{\mathrm{p}} \rceil \lambda_f^{\mathrm{p}} \frac{\partial f^{\mathrm{p}}}{\partial E}}, \tag{18}$$

yielding

$$\dot{\mathrm{P}}^{\mathrm{i}} = \left(1 - \left\lceil \lfloor h^{\mathrm{p}} \rceil \lceil \overset{*}{h}{}^{\mathrm{p}} \rfloor + \lceil f^{\mathrm{p}} \rfloor \right\rfloor \right) \lfloor f^{\mathrm{p}} \rceil \lfloor \overset{*}{f}{}^{\mathrm{p}} \rceil \lambda_f^{\mathrm{p}} \frac{\partial f^{\mathrm{p}}}{\partial E}, + \left\lceil \lfloor h^{\mathrm{p}} \rceil \lceil \overset{*}{h}{}^{\mathrm{p}} \rfloor + \lceil f^{\mathrm{p}} \rfloor \right\rfloor \lambda_h^{\mathrm{p}} \frac{\partial h^{\mathrm{p}}}{\partial P^{\mathrm{i}}}. \tag{19}$$

In a similar fashion, we introduce the criteria

$$f^{\mathrm{f}}(\sigma, S^{\mathrm{f}}) = |\sigma - c^{\mathrm{f}} S^{\mathrm{f}}| - \hat{\sigma}_{\mathrm{c}}(E, P^{\mathrm{i}}), \tag{20}$$

$$h^{\mathrm{f}}(S^{\mathrm{f}}, P^{\mathrm{i}}) = |S^{\mathrm{f}}| - (S_{\mathrm{sat}} - |S^{\mathrm{p}}|), \tag{21}$$

where c^{f} is a non-negative constant. In general, the critical stress $\hat{\sigma}_{\mathrm{c}}$ for the onset of ferroelastic changes depends on the loading history via E, P^{i}. The term in brackets in Eq. (21) assures that the magnitude of the total remanent strain never exceeds its saturation value: $|S^{\mathrm{i}}| = |S^{\mathrm{p}} + S^{\mathrm{f}}| \leqslant S_{\mathrm{sat}}$ for $h^{\mathrm{f}} \leqslant 0$. With the definitions

$$\overset{*}{f}{}^{\mathrm{f}} = \frac{\mathrm{d}}{\mathrm{d}t} f^{\mathrm{f}} \bigg|_{\dot{S}^{\mathrm{f}}=0,} \qquad \overset{*}{h}{}^{\mathrm{f}} = \frac{\mathrm{d}}{\mathrm{d}t} h^{\mathrm{f}} \bigg|^{\mathrm{f}}_{\dot{S} = \lfloor f^{\mathrm{f}} \rceil \lfloor \overset{*}{f}{}^{\mathrm{f}} \rceil \lambda_f^{\mathrm{f}} \frac{\partial f^{\mathrm{f}}}{\partial \sigma}}, \tag{22}$$

we get

$$\dot{S}^{\mathrm{f}} = \left(1 - \left\lceil \lfloor h^{\mathrm{f}} \rceil \lceil \overset{*}{h}{}^{\mathrm{f}} \rfloor + \lceil f^{\mathrm{f}} \rfloor \right\rfloor \right) \lfloor f^{\mathrm{f}} \rceil \lfloor \overset{*}{f}{}^{\mathrm{f}} \rceil \lambda_f^{\mathrm{f}} \frac{\partial f^{\mathrm{f}}}{\partial \sigma} + \left\lceil \lfloor h^{\mathrm{f}} \rceil \lceil \overset{*}{h}{}^{\mathrm{f}} \rfloor + \lceil f^{\mathrm{f}} \rfloor \right\rfloor \lambda_h^{\mathrm{f}} \frac{\partial h^{\mathrm{f}}}{\partial S^{\mathrm{f}}} \tag{23}$$

for the ferroelastic strain evolution. Again, λ_h^{f} and λ_f^{f} have to be determined by consistency conditions, this time $(\mathrm{d}h^{\mathrm{f}}/\mathrm{d}t) = 0$ and $(\mathrm{d}f^{\mathrm{f}}/\mathrm{d}t) = 0$, respectively.

Schäufele and Härdtl (1996) have found a linear dependence of the coercive stress on a superposed electric field, and because of this we assume

$$\hat{\sigma}_{\mathrm{c}}(E, P^{\mathrm{i}}) = \left\langle \sigma_{\mathrm{c}} + n \frac{E}{E_c} \frac{P^{\mathrm{i}}}{|P^{\mathrm{i}}|} \right\rangle, \tag{24}$$

where $\langle x \rangle = 0$ for $x \leqslant 0$ and $\langle x \rangle = x$ for $x \geqslant 0$. The constant σ_{c} is the coercive stress in the absence of an electric field, and the constant n determines the extent of the influence of the electric field on the effective coercive stress $\hat{\sigma}_{\mathrm{c}}$. An appropriate assumption for $\hat{P}_{\mathrm{sat}}$ allows one to take into account the phenomenon of mechanical depolarization. One simple choice is

$$\hat{\mathrm{P}}_{\mathrm{sat}}(\sigma, E, P^{\mathrm{i}}) = \hat{\mathrm{P}}^{\mathrm{exp}}_{\mathrm{sat}}(\sigma, E, P^{\mathrm{i}}) = P_{\mathrm{sat}}\, \mathrm{e}^{-\langle -\sigma - \hat{\sigma}_{\mathrm{c}}(E, P^{\mathrm{i}}) \rangle / m}, \tag{25}$$

where the constant P_{sat} is the maximum remanent polarization introduced before and m is a positive constant governing the progress of mechanical depolarization. According to this definition, compressive

stresses of sufficient magnitude lead to a gradual reduction of the remanent polarization. In this paper, we adopt the choice

$$\hat{\mathbf{P}}_{\mathrm{sat}}(\sigma,E,P^{\mathrm{i}})=\hat{\mathbf{P}}^{\mathrm{lin}}_{\mathrm{sat}}(\sigma,E,P^{\mathrm{i}})=(P_{\mathrm{sat}}-P_{\delta})\left\langle 1-\frac{1}{m}\langle -\sigma-\hat{\sigma}_{\mathrm{c}}(E,P^{\mathrm{i}})\rangle\right\rangle+P_{\delta}, \tag{26}$$

allowing for considering a fraction $P_{\delta}\geqslant 0$ of the remanent polarization which will persist compressive stresses of arbitrary magnitude.

Fig. 1 shows some typical multilinearly approximated hystereses obtained with the help of our model. The material constants were chosen according to Table 1 approximating typical PZT ceramics very roughly. In principle, the large signal parameters may be determined as follows: The constants E_{c} (onset),

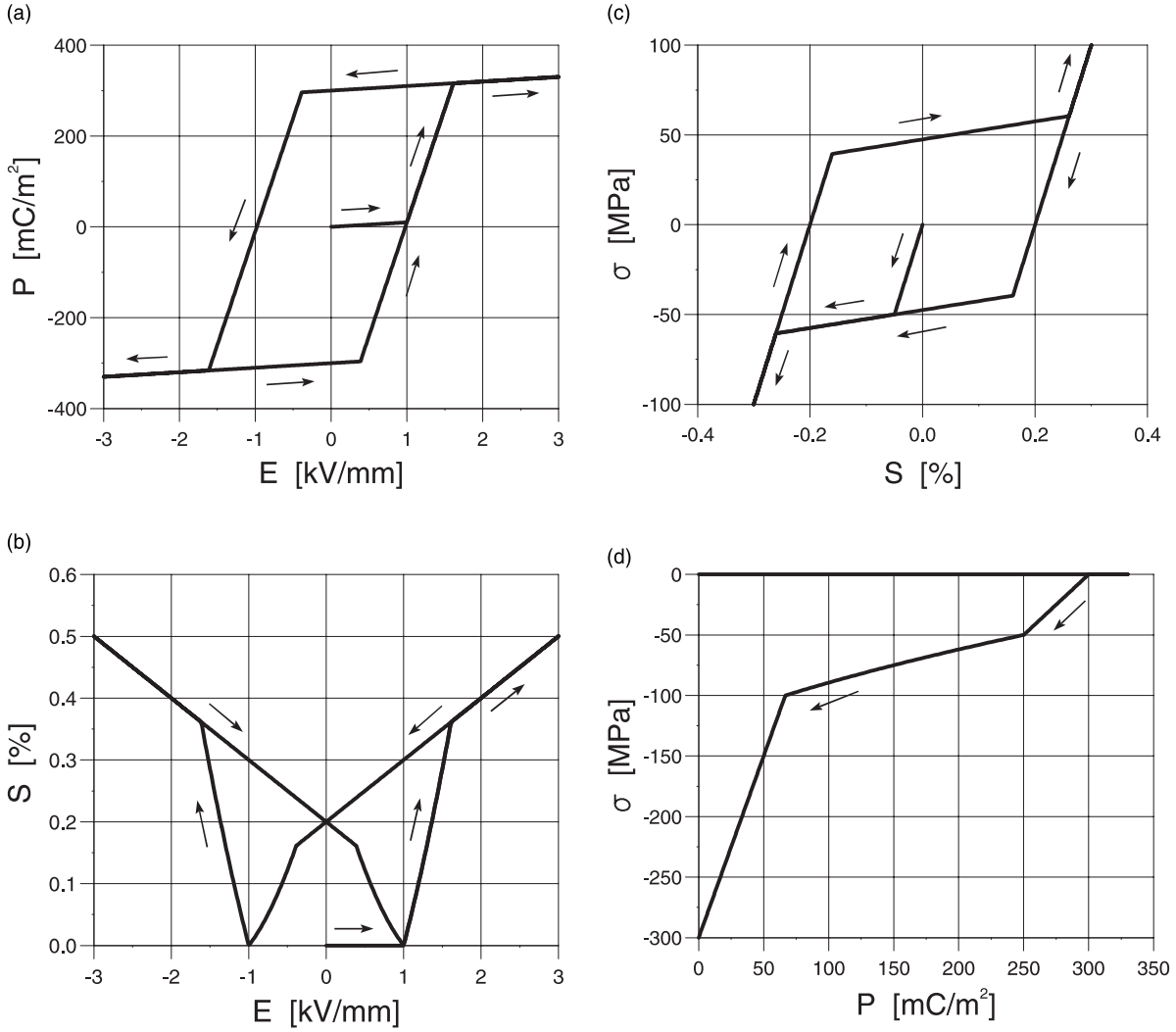

Fig. 1. Multilinear approximation of some hysteresis phenomena observed in piezoceramics: (a) dielectric hysteresis (b) butterfly hysteresis (c) ferroelastic hysteresis and (d) mechanical depolarization.

Table 1
Values of the material constants used to simulate Figs. 1 and 2

E_c	(kV/mm)	1.0
P_{sat}	(mC/m^2)	300
d	(mm/kV)	0.001
ϵ	(mC/kVm)	0.01
c^p	(kVm/mC)	2.0
S_{sat}	(%)	0.2
Y	(GPa)	100
σ_c	(MPa)	50.0
c^f	(GPa)	5.3
m	(MPa)	50
n	(MPa)	30.0
P_δ	(mC/m^2)	100

P_{sat} (remanent value), c^p (slope), and S_{sat} (remanent value) can be taken from the classical dielectric and butterfly hystereses, σ_c (onset) and c^f (slope) describe the ferroelastic behavior under uniaxial compression, P_δ (remaining value) and m (slope) govern the depolarization behavior while n (onset) characterizes the influence of a superposed electric field on a depolarizing mechanical compression load.

The first polarization curve in the dielectric hysteresis in Fig. 1a starts at the origin and $f^p \leqslant 0$ holds and, likewise, $h^p \leqslant 0$ until the coercive field E_c is reached. From now on, $f^p(t) = 0$ on account of the consistency condition and irreversible poling takes place. For $P^i = P_{sat}$, a second kink is observed and afterwards P experiences reversible changes only, since $h^p(t) = 0$ has now to be satisfied. Due to the isotropy assumption for ϵ, the slopes of the first and the third periods are the same ($= \epsilon$). The slope of the intermediate phase of irreversible polarization change depends additionally on c^p. If the electric field is reversed, we eventually observe poling in the new direction of the electric field. Finally, upon reversing the electric field again, the hysteresis loop is closed.

The butterfly hysteresis in Fig. 1b starts from an unpoled state, and no strain is electrically induced as long as the coercive field has not been reached, since $P^i = 0$ in that case. For values of the electric field beyond E_c, the remanent polarization grows and S changes quadratically with respect to the electric field. In the fully poled state, a linear piezoelectric range is reached, the slope of which is given by d. Unloading yields the saturation strain S_{sat}. Depolarization and new polarization after reversing the electric field lead first to a removal and then again to a rapid increase in irreversible deformation. Finally, a second piezoelectric range is reached.

In the ferroelastic hysteresis in Fig. 1c, we recognize a bilinear approximation with three different ranges: a first range of reversible response, an intermediate phase during which ferroelastic remanent strain develops, and a saturated part corresponding to the maximum remanent strain. Because of the isotropy assumption (5b), both the slopes of the first and the third parts of the mechanical response are equal to Y. The tangent modulus of the intermediate phase of irreversible deformation depends additionally on c^f. Note, that due to a simplified formulation of the saturation criterion h^f in Eq. (21), the ferroelastic hysteresis is symmetrical with respect to the origin.

In Fig. 1d, the horizontal line represents an initial poling process. After removing the electric field, thereby reducing P to $P^i = P_{sat}$, an increasing compressive stress is applied, leading first to linear piezoelectric changing and for $\sigma < -\sigma_c$ to mechanical depolarization. Since a certain degree P_δ of the remanent polarization remains, there also survives some piezoelectricity. For a detailed discussion of the uniaxial model response, we refer to Kamlah and Tsakmakis (1999) and Kamlah et al. (1997), again.

In principle, a representation of the material behavior as realistic as possible is desirable. However, a detailed constitutive model involves a large number of material constants and functions making it hard to identify the influence of a certain parameter on the behavior of the structure under consideration. In the

current situation at the beginning of the scientific discussion about piezoceramics structures, we consider it more instructive to apply a simple model depending only on a few significant large signal parameters.

2.3. Tensorial generalization of the evolution laws

In principle, the tensorial generalization of the evolution laws is facilitated by replacing in the functions (14), (15), (20), (21), (24), and (26), the uniaxial quantities by appropriate tensorial invariants. Then, normality and consistency conditions lead to the differential equations for $\vec{\mathrm{P}}^{\mathrm{i}}$ and $\boldsymbol{S}^{\mathrm{f}}$.

The invariants have to be chosen such that the previous uniaxial formulation is contained as a special case for uniaxial loadings. In this sense, it is quite straightforward to replace the absolute magnitudes in Eqs. (14), (15), (20), and (21) by tensor norms of the corresponding rank:

$$f^{\mathrm{p}}(\vec{\mathrm{E}},\vec{\mathrm{P}}^{\mathrm{i}}) = \left\|\vec{\mathrm{E}} - c^{\mathrm{p}}\vec{\mathrm{P}}^{\mathrm{i}}\right\| - E_{\mathrm{c}}, \tag{27}$$

$$h^{\mathrm{p}}(\boldsymbol{T},\vec{\mathrm{E}},\vec{\mathrm{P}}^{\mathrm{i}}) = \left\|\vec{\mathrm{P}}^{\mathrm{i}}\right\| - \hat{\mathrm{P}}_{\mathrm{sat}}(\boldsymbol{T},\vec{\mathrm{E}},\vec{\mathrm{P}}^{\mathrm{i}}), \tag{28}$$

$$f^{\mathrm{f}}(\boldsymbol{T},\vec{\mathrm{E}},\vec{\mathrm{P}}^{\mathrm{i}},\boldsymbol{S}^{\mathrm{f}}) = \sqrt{\tfrac{3}{2}}\left\|(\boldsymbol{T} - c^{\mathrm{f}}\boldsymbol{S}^{\mathrm{f}})^{D}\right\| - \hat{\sigma}_{\mathrm{c}}(\vec{\mathrm{E}},\vec{\mathrm{P}}^{\mathrm{i}}), \tag{29}$$

$$h^{\mathrm{f}}(\vec{\mathrm{P}}^{\mathrm{i}},\boldsymbol{S}^{\mathrm{f}}) = \sqrt{\tfrac{2}{3}}\left\|\boldsymbol{S}^{\mathrm{f}}\right\| - \left(S_{\mathrm{sat}} - \sqrt{\tfrac{2}{3}}\left\|\boldsymbol{S}^{\mathrm{p}}\right\|\right). \tag{30}$$

The normalizing factors in Eqs. (29) and (30) were chosen for convenience. Taking the deviator in f^{f} makes sure that by application of the normality rule the evolution of $\boldsymbol{S}^{\mathrm{f}}$ is deviatoric as demanded at the end of Section 2.1.

Furthermore, it seems to be an obvious choice to replace the n-term in Eq. (24) by a corresponding vectorial inner product:

$$\hat{\sigma}_{\mathrm{c}}(\vec{\mathrm{E}},\vec{\mathrm{P}}^{\mathrm{i}}) = \left\langle \sigma_{\mathrm{c}} + n\frac{\vec{\mathrm{E}}}{E_{\mathrm{c}}}\cdot\vec{\mathrm{e}}_{\mathrm{P}^{\mathrm{i}}}\right\rangle. \tag{31}$$

Finally, we write instead of Eq. (26)

$$\hat{\mathrm{P}}_{\mathrm{sat}}(\boldsymbol{T},\vec{\mathrm{E}},\vec{\mathrm{P}}^{\mathrm{i}}) = (P_{\mathrm{sat}} - P_{\delta})\left\langle 1 - \frac{1}{m}\left\langle -\tfrac{3}{2}\vec{\mathrm{e}}_{\mathrm{P}^{\mathrm{i}}}\cdot\boldsymbol{T}^{D}\cdot\vec{\mathrm{e}}_{\mathrm{P}^{\mathrm{i}}} - \hat{\sigma}_{\mathrm{c}}(E,P^{\mathrm{i}})\right\rangle\right\rangle + P_{\delta}. \tag{32}$$

For a motivation of the $\boldsymbol{T}^{D}$ term in this equation, we consider a poled state with $\vec{\mathrm{e}}_{\mathrm{P}^{\mathrm{i}}} = \vec{\mathrm{e}}_3$ and $\vec{\mathrm{E}} = \vec{0}$. For the case of a uniaxial stress state T_{33} acting in the x_3-direction, we obtain

$$\left\langle -\tfrac{3}{2}\vec{\mathrm{e}}_{\mathrm{P}^{\mathrm{i}}}\cdot\boldsymbol{T}^{D}\cdot\vec{\mathrm{e}}_{\mathrm{P}^{\mathrm{i}}} - \sigma_{\mathrm{c}}\right\rangle = \left\langle -T_{33} - \sigma_{\mathrm{c}}\right\rangle, \tag{33}$$

while a biaxial stress state $T_{11} = T_{22}$ acting in the x_1–x_2 plane yields

$$\left\langle -\tfrac{3}{2}\vec{\mathrm{e}}_{\mathrm{P}^{\mathrm{i}}}\cdot\boldsymbol{T}^{D}\cdot\vec{\mathrm{e}}_{\mathrm{P}^{\mathrm{i}}} - \sigma_{\mathrm{c}}\right\rangle = \left\langle T_{11} - \sigma_{\mathrm{c}}\right\rangle. \tag{34}$$

Thus, our choice of $\hat{\mathrm{P}}_{\mathrm{sat}}$ corresponds to the hypothesis that compressive stresses in the direction of poling as well as tensile stresses perpendicular to the direction of poling can lead to mechanical depolarization.

For a compact formulation of the evolution equations, we now introduce the abbreviations,

$$F^{\mathrm{i}} = \lfloor f^{\mathrm{i}}\rceil\lfloor \overset{*}{f}{}^{\mathrm{i}}\rceil, \quad H^{\mathrm{i}} = \left\lceil \lfloor h^{\mathrm{i}}\rceil\lceil \overset{*}{h}{}^{\mathrm{i}}\rfloor\lceil f^{\mathrm{i}}\rfloor\right\rfloor, \quad i = p,f. \tag{35}$$

While $F = 1$ means that the related f-criterion is fulfilled, indicates $H = 1$ that the corresponding h-criterion is in effect. Then, applying normality as before, we obtain

$$\dot{\vec{\mathrm{P}}} = (1 - H^{\mathrm{p}})F^{\mathrm{p}}\lambda_f^{\mathrm{p}}\,\frac{\partial f^{\mathrm{p}}}{\partial \vec{\mathrm{E}}} + H^{\mathrm{p}}\lambda_h^{\mathrm{p}}\frac{\partial h^{\mathrm{p}}}{\partial \vec{\mathrm{P}}^{\mathrm{i}}}, \tag{36}$$

$$\dot{\boldsymbol{S}}^{\mathrm{f}} = (1 - H^{\mathrm{f}})F^{\mathrm{f}}\lambda_f^{\mathrm{f}}\frac{\partial f^{\mathrm{f}}}{\partial \boldsymbol{T}} + H^{\mathrm{f}}\lambda_h^{\mathrm{f}}\frac{\partial h^{\mathrm{f}}}{\partial \boldsymbol{S}^{\mathrm{f}}}, \tag{37}$$

where the factors of proportionality λ_f^{p}, λ_h^{p}, λ_f^{f}, and λ_h^{f} have to be determined by the consistency conditions $(\mathrm{d}f^{\mathrm{p}}/\mathrm{d}t) = 0$, $(\mathrm{d}h^{\mathrm{p}}/\mathrm{d}t) = 0$, $(\mathrm{d}f^{\mathrm{f}}/\mathrm{d}t) = 0$, and $(\mathrm{d}h^{\mathrm{f}}/\mathrm{d}t) = 0$, respectively.

According to the above formulation of the evolution law (36), $\vec{\mathrm{P}}^{\mathrm{i}}$ is constant, once a fully poled state is reached, in the x_1-direction for instance, and no stress is acting. However, we want to allow for a rotation of the saturated remanent polarization vector, if additionally to the originally poling field, a perpendicular electric field component, e.g. $E_2 \neq 0$, is superposed. For this purpose, we introduce the second-order projection tensor,

$$\boldsymbol{P}_{\mathrm{b}} = \boldsymbol{I} - \vec{\mathrm{e}}_{\mathrm{b}} \otimes \vec{\mathrm{e}}_{\mathrm{b}}, \qquad \vec{\mathrm{b}} = \frac{\partial h^{\mathrm{p}}}{\partial \vec{\mathrm{P}}^{\mathrm{i}}} \tag{38}$$

with the property

$$\frac{\partial h^{\mathrm{p}}}{\partial \vec{\mathrm{P}}^{\mathrm{i}}} \cdot (\boldsymbol{P}_b \cdot \vec{\mathrm{a}}) = 0 \quad \text{for arbitrary } \vec{\mathrm{a}}. \tag{39}$$

Thus, in its geometrical interpretation, $\boldsymbol{P}_{\mathrm{b}}$ projects any vector on a tangent plane to the surface $h^{\mathrm{p}}(\vec{\mathrm{P}}^{\mathrm{i}}) = 0$. We exploit this property, by adding the term $\boldsymbol{P}_b \cdot (F^{\mathrm{p}}\lambda_f^{\mathrm{p}}\partial f^{\mathrm{p}}/\partial \vec{\mathrm{E}})$ to the right-hand side of Eq. (36), in order to extend the model by the effect of the rotation of a saturated remanent polarization state. Then, the evolution law for $\vec{\mathrm{P}}^{\mathrm{i}}$ can be written as

$$\dot{\vec{\mathrm{P}}}^{\mathrm{i}} = \left(\boldsymbol{I} - H^{\mathrm{p}}\vec{\mathrm{e}}_{\mathrm{b}} \otimes \vec{\mathrm{e}}_{\mathrm{b}}\right) \cdot \left(F^{\mathrm{p}}\lambda_f^{\mathrm{p}}\frac{\partial f^{\mathrm{p}}}{\partial \vec{\mathrm{E}}}\right) + H^{\mathrm{p}}\lambda_h^{\mathrm{p}}\frac{\partial h^{\mathrm{p}}}{\partial \vec{\mathrm{P}}^{\mathrm{i}}}. \tag{40}$$

In fact, in Fig. 2, we observe that the saturated remanent polarization vector is rotated if after an initial step of poling in the x_1-direction an additional electric field component in the x_2-direction is superposed in the absence of any stress. P_2^{i} grows at the expense of P_1^{i} such that at each instant, the condition $\left\|\vec{\mathrm{P}}^{\mathrm{i}}\right\| = \sqrt{P_1^{\mathrm{i}2} + P_2^{\mathrm{i}2}} = P_{\mathrm{sat}} = \text{const}$ is fulfilled.

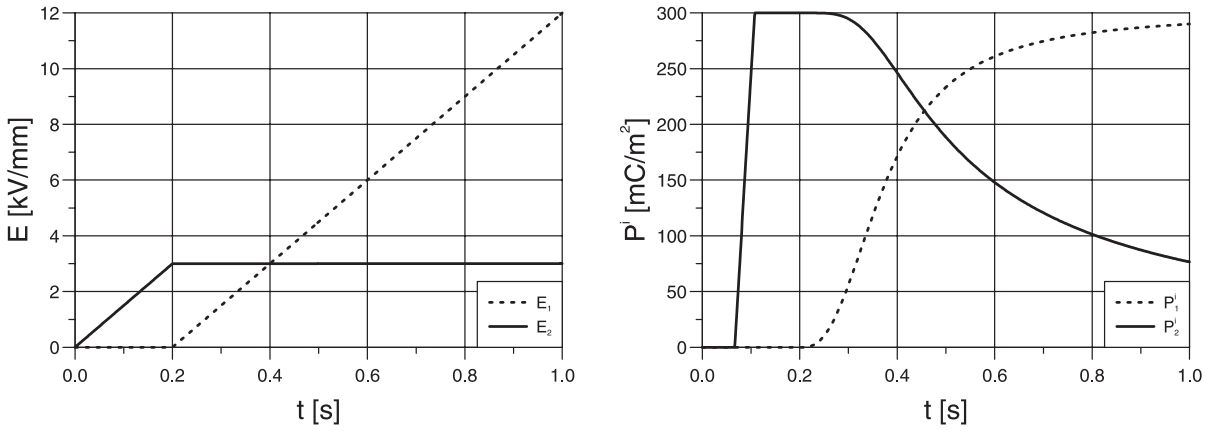

Fig. 2. Rotation of a saturated remanent polarization state: After poling took place first in the x_1-direction until saturation, additionally an electric field component in the x_2-direction is superposed. It can clearly be seen that the 2-component of $\vec{\mathrm{P}}^{\mathrm{i}}$ starts to grow at the expense of P_1^{i}.

Finally, merely as an act of formal analogy, we may extend the evolution equation for $\boldsymbol{S}^{\mathrm{f}}$ by a corresponding projection term. With the help of the fourth-order projection tensor

$$\mathbb{P} = \mathbb{I} - \boldsymbol{N}^{\mathrm{f}} \otimes \boldsymbol{N}^{\mathrm{f}}, \quad \boldsymbol{N}^{\mathrm{f}} = \frac{\partial h^{\mathrm{f}}/\partial \boldsymbol{S}^{\mathrm{i}}}{\left\|\partial h^{\mathrm{f}}/\partial \boldsymbol{S}^{\mathrm{i}}\right\|}, \tag{41}$$

a term $\mathbb{P}{:}(F^{\mathrm{f}}\lambda_f^{\mathrm{f}}\partial f^{\mathrm{f}}/\partial \boldsymbol{T})$ can be added to the right-hand side of Eq. (37), yielding

$$\dot{\boldsymbol{S}}^{f} = \left(\mathbb{I} - H^{\mathrm{f}}\boldsymbol{N}^{\mathrm{f}} \otimes \boldsymbol{N}^{\mathrm{f}}\right) : \left(F^{\mathrm{f}}\lambda_f^{\mathrm{f}}\frac{\partial f^{\mathrm{f}}}{\partial \boldsymbol{T}}\right) + H^{\mathrm{f}}\lambda_h^{\mathrm{f}}\frac{\partial h^{\mathrm{f}}}{\partial \boldsymbol{S}^{\mathrm{f}}}. \tag{42}$$

However, since this extension of the evolution law for $\boldsymbol{S}^{\mathrm{f}}$ lacks physical motivation, it might be disregarded.

Thus, the tensorial generalization of the evolution laws for the internal variables has been realized by quite straightforward application of tensorial invariants. No additional material constant was introduced. This is important because multiaxial experiments that would be needed in order to identify parameters describing multiaxial behavior alone are not available as yet and will be very difficult. The evolution equations were derived from a few scalar criteria with clear physical meaning by means of normality rules and consistency conditions. This principle procedure for the construction of the evolution laws for the internal variables is given below.

- onset of switching processes

$$f^{\mathrm{p}}(\vec{\mathrm{E}}, \vec{\mathrm{P}}^{\mathrm{i}}) = 0 \leftrightarrow |E| = E_{\mathrm{c}},$$

$$f^{\mathrm{f}}(\boldsymbol{T}, \vec{\mathrm{E}}, \vec{\mathrm{P}}^{\mathrm{i}}, \boldsymbol{S}^{\mathrm{f}}) = 0 \leftrightarrow |\sigma| = \sigma_{\mathrm{c}},$$

- fully switched domain structure

$$h^{\mathrm{p}}(\boldsymbol{T}, \vec{\mathrm{E}}, \vec{\mathrm{P}}^{\mathrm{i}}) = 0 \leftrightarrow |P^{\mathrm{i}}| = P_{\mathrm{sat}},$$

$$h^{\mathrm{f}}(\vec{\mathrm{P}}^{\mathrm{i}}, \boldsymbol{S}^{\mathrm{f}}) = 0 \leftrightarrow |S^{\mathrm{i}}| = S_{\mathrm{sat}},$$

- normality and consistency condition for $f^{\mathrm{p}} = 0$ and $h^{\mathrm{p}} = 0$

$$\Rightarrow \dot{\vec{\mathrm{P}}}^{\mathrm{i}} = g_{\mathrm{P}^{\mathrm{i}}}(\boldsymbol{S}, \vec{\mathrm{E}}, \vec{\mathrm{P}}^{\mathrm{i}}, \boldsymbol{S}^{\mathrm{f}}, \dot{\boldsymbol{S}}, \dot{\vec{\mathrm{E}}}) \quad \text{see Eq. (40)},$$

- normality and consistency condition for $f^{\mathrm{f}} = 0$ and $h^{\mathrm{f}} = 0$

$$\Rightarrow \dot{\boldsymbol{S}}^{\mathrm{f}} = g_{S^{\mathrm{f}}}(\boldsymbol{S}, \vec{\mathrm{E}}, \vec{\mathrm{P}}^{\mathrm{i}}, \boldsymbol{S}^{\mathrm{f}}, \dot{\boldsymbol{S}}, \dot{\vec{\mathrm{E}}}) \quad \text{see Eq. (42)}.$$

While it is attractive to arrive at fully three-dimensional evolution equations in such a simple manner, it must not be overseen that the numerical treatment of the involved loading conditions during integration is delicate. (For decades, this topic has given rise for ongoing discussions in the field of phenomenological modeling of plasticity, e.g. Dafalias and Popov (1976), Simo (1988)). Note, that application of the consistency conditions implies that our model is rate independent.

3. Finite element implementation

In general, the system of electro-mechanical field equations is given by the geometrically non-linear mechanical momentum balances combined with the Maxwell equations (Hutter and van de Ven, 1978; Maugin, 1988; the debate about the formulation of this general theory seems not yet to be settled). For the technical applications we are aiming at, the essentially simplified geometrically linear, quasi-electrostatic theory of a deformable dielectric given by the balance of linear momentum together with the Gaussian law is usually applied (Maugin, 1988; Parton and Kudryavtsev, 1988; Suo et al., 1992), see also many other of

the publications cited in this paper. Neglecting volume charge and volume force densities, this set of equations reads (ρ: *mass density*)

$$\operatorname{div}\vec{D} = 0, \tag{43}$$

$$\operatorname{div}\boldsymbol{T} = \rho\ddot{\vec{u}}, \tag{44}$$

where

$$\vec{D} = \epsilon_0\vec{E} + \vec{P} \tag{45}$$

is the *dielectric displacement vector*. Containing much more unknowns than equations, this system has to be closed by relations describing the properties of the material under consideration. Here, of course, we apply the constitutive law for ferroelectric and ferroelastic hysteresis effects presented in Section 2.

For a particular electro-mechanical problem, the resulting systems of equations has to be solved for boundary conditions for the electric potential, φ, or surface charge density, $\vec{D}\cdot\vec{n}$, as well as for the displacement, $\vec{u}$, or surface force density, $\boldsymbol{T}\cdot\vec{n}$ ($\vec{n}$: unit surface normal). Even though our constitutive law represents the true behavior in a simplifying manner, such boundary value problems cannot be solved analytically in general. Therefore, numerical methods are needed. In structural mechanics, the finite element method is probably the most popular choice, as it can be applied very flexibly to a wide range of geometries (for the weak formulation of the theory needed for the finite element formulation as well as the finite element formulation itself see Allik and Hughes (1970), Gaudenzi and Bathe (1995), Hom and Shankar (1995), Gong and Suo (1996), Ghandi and Hagood (1997), Chen and Lynch (1999)).

For the finite element implementation of our model, we decided for the non-linear multipurpose finite element code PSU, designed for scientific applications. This public domain code runs on UNIX-like operating systems and is provided by the Institute of Statics and Dynamics of Aerospace Structures of the Stuttgart University. For more information see Lange (1993), Lübbing et al. (1994), and the web page http://www.isd.uni-stuttgart.de/arbeitsgruppen/psu-www/index.html. The source code can be downloaded from the ftp-server ftp.isd.uni-stuttgart.de, directory: pub/psu.

For the solution of electro-mechanical boundary value problems, geometrically linear four node plane strain and axisymmetric elements are available. The classical linear piezoelectric constitutive law is already implemented (Lübbing, 1997). In principle, what we had to do was to replace the existing implementation of the linear constitutive law by an implementation of our hysteresis law.

3.1. The user defined material routine M_NLFERRO_EM

In this subsection, we briefly present the numerical integration scheme of our model and the software package M_NLFERRO_EM for the implementation in PSU (this package is not included in the download mentioned above). For a detailed description, see Böhle (1999).

The constitutive model of Section 2 can be written as a system of ordinary differential equations with respect to time. The factors of proportionality λ_f^{p}, λ_h^{p}, λ_f^{f}, and λ_h^{f} were calculated analytically from the corresponding consistency conditions for the case of prescribed electric field $\vec{E}$ and strain $\boldsymbol{S}$. For the numerical integration of the resulting system of differential equations, we chose a highly accurate explicit Runge–Kutta scheme. The points of changing from one loading condition to another are identified by cutting back subincrements iteratively until the time instant of the change is identified with sufficient accuracy.

There are two options available for passing the material-dependent contribution to the tangent stiffness operator to the non-linear finite element solver. The first one is obtained by numerical differentiation of the constitutive law by symmetric difference quotients. As the second approximate choice, by means of the

tensors ϵ, $\mathbb{C}$, and $\mathbb{d}$ according to Eqs. 5(a), (b) and (6), respectively, a tangent stiffness operator of the structure of linear piezoelectricity is constructed.

We are well aware that there are more efficient and more stable integration algorithms available, as well as there are more sophisticated realizations for the tangent stiffness operator possible. However, our first priority is to obtain a working tool by methods as simple and transparent as possible. This is supposed to allow us to check the gain of physical insight in the behavior of piezoceramic devices brought about by the application of the more general constitutive law. Granted a positive result, further efforts for optimizing the mathematical and numerical performance of model and routine, respectively, are justified.

In this paper, we realize the electro-mechanical finite element analysis by a two-step scheme (Fig. 3). Since the response of our constitutive model is history dependent, the loading history has to be subdivided in sufficiently small increments and evaluated at the resulting discrete instants $t_I \in \{t_0, t_1, \ldots, t_e\}$ in order to loose no information.

In the first step, the purely dielectric boundary value problem is solved. For the given boundary conditions with respect to the electric potential or the surface charge density, the Gaussian law is solved yielding for each increment $t_I \in \{t_0, t_1, \ldots, t_e\}$ of the loading history the corresponding values $\varphi(\vec{x}_K, t_I)$ of the electric potential at each node $\vec{x}_K$. In this way, a purely dielectrically calculated solution $\vec{P}^{i}_{diel}(\vec{x}_K, t_I)$ for the remanent polarization is obtained.

Now, in the second step, the electro-mechanical stress analysis is carried out. Besides the mechanical boundary conditions for displacement or surface force density, the electric potential history $\varphi(\vec{x}_K, t_I)$ is prescribed for each node $\vec{x}_K$ of the finite element net at each increment t_I. The Gaussian law and the balance of linear momentum are solved yielding all electro-mechanical fields of interest: $\boldsymbol{T}, \boldsymbol{S}, \vec{E}, \vec{P}, \vec{P}^{i}, \boldsymbol{S}^{p}, \boldsymbol{S}^{f}$.

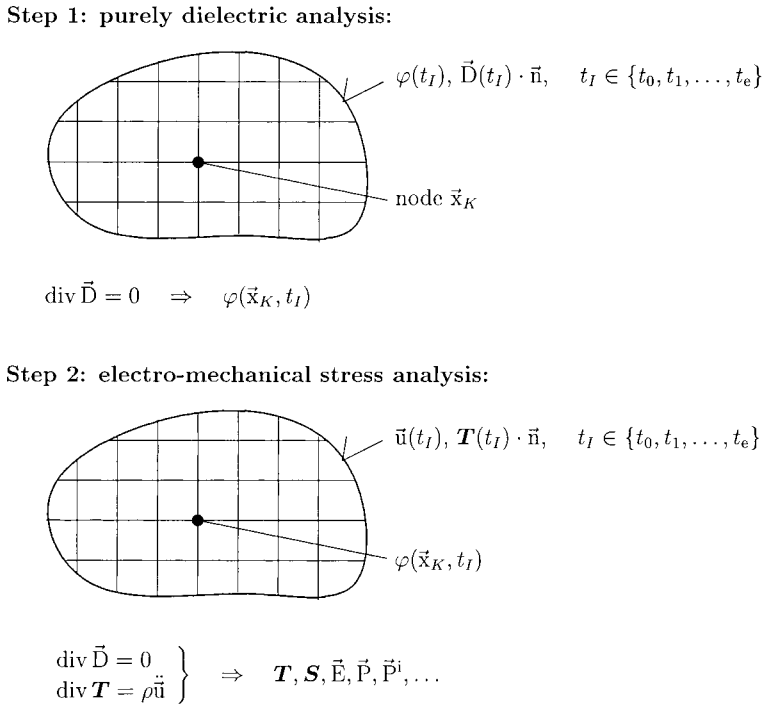

Fig. 3. Two-step scheme for the electro-mechanical analysis: the history of the field of the electric potential obtained in the first step is prescribed in the second step of the electro-mechanical stress analysis.

In this way it is assured that the modified electric quantities derived from the coupled material model fulfil the Gaussian law, too.

Obviously, not the fully coupled problem is solved, since the mechanical boundary conditions have no influence on the solution for the electric potential. However, this splitting up of the problem seems to be justified in the sense of an approximation, as it can be expected, that the coupling in the direction from the mechanical boundary conditions towards the dielectric solution is much weaker than the other way around (for an investigation on this question in the context of electrostrictive behavior, see Gong (1995)). Please note, that such a two-step procedure is very common in thermomechanical analyses. Implementing the fully coupled solution, we experienced so far convergence problems with the global Newton iteration, the reason for which cannot yet be identified.

3.2. Verification of the implementation

One necessary criterion for a successful finite element implementation of a constitutive model is of course that for homogenous uniaxial loadings the uniaxial response of the model must be obtained. In this sense, we now consider uniaxial electro-mechanical loadings of a cylinder described by a single axisymmetric element (Fig. 4). Note that in this case the first dielectric step is not necessary, since the electric potential at each of the four nodes is determined by the electric boundary conditions and thus is known a priori. For all finite element calculations, the set of material constants given in Table 2 was used. They were chosen such that the behavior of a typical soft PZT (e. g. PIC 151) is represented approximately.

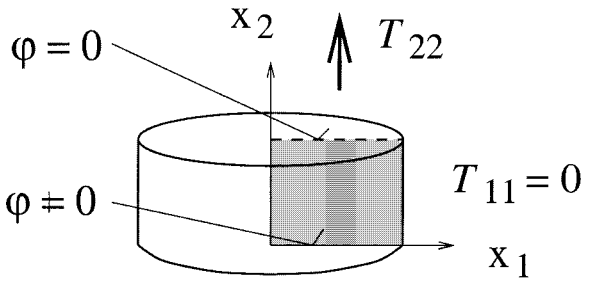

Fig. 4. Uniaxial electro-mechanical loading of a solid cylinder represented by a single axisymmetric finite element.

Table 2
Values of the material constants chosen for the finite element calculations

ϵ	1.5×10^{-8}	C/(V m)
$d_{\parallel}$	3.5×10^{-10}	m/V
E_c	1.0×10^{6}	V/m
σ_c	5.0×10^{7}	N/m^2
n	5.0×10^{7}	N/m^2
Y	8.0×10^{10}	N/m^2
$d_{\perp}$	-1.4×10^{-11}	m/V
P_{sat}	0.3	C/m^2
S_{sat}	0.002	–
m	1.5×10^{8}	N/m^2
ν	0.35	–
$d_{=}$	5.2×10^{-10}	m/V
c^p	2.0×10^{6}	V m/C
c^f	5.0×10^{9}	N/m^2
P_{δ}	0.1	C/m^2

As the first example, we consider the strains induced by electric cycling in Fig. 5. On the left-hand side, we see the common butterfly hysteresis in poling direction, where the slope of the poled linear piezoelectric behavior due to the inverse piezoelectric effect is determined by $d_{\parallel}$. On the right-hand side of Fig. 5, the corresponding transverse strains are shown. They are negative, indicating contraction. The remanent transverse strains after removing the electric field are half of the remanent strain in the poling direction due to the assumed deviatoric changing of the remanent strains. The slope of the linear piezoelectric range in the transverse direction is given by $d_{\perp}$.

We now consider electric cycling for different values of a superposed mechanical stress in Fig. 6. The solid curves represent the response for the dielectric displacement and the strain for zero mechanical stress and thus correspond to the related curves in Figs. 1 and 5.

The case of a superposed tensile stress is represented by the dotted lines. In the dielectric hysteresis on the left-hand side of Fig. 6, we observe an additional contribution to the dielectric displacement in the fully poled range due to the direct piezoelectric effect (see the first term in Eq. (12)). The strain response on the right of Fig. 6 is significantly modified. First of all, we recognize an additional tensile strain due to the initial elastic response to the stress. More interestingly, the butterfly hysteresis exhibits only degenerated tips.

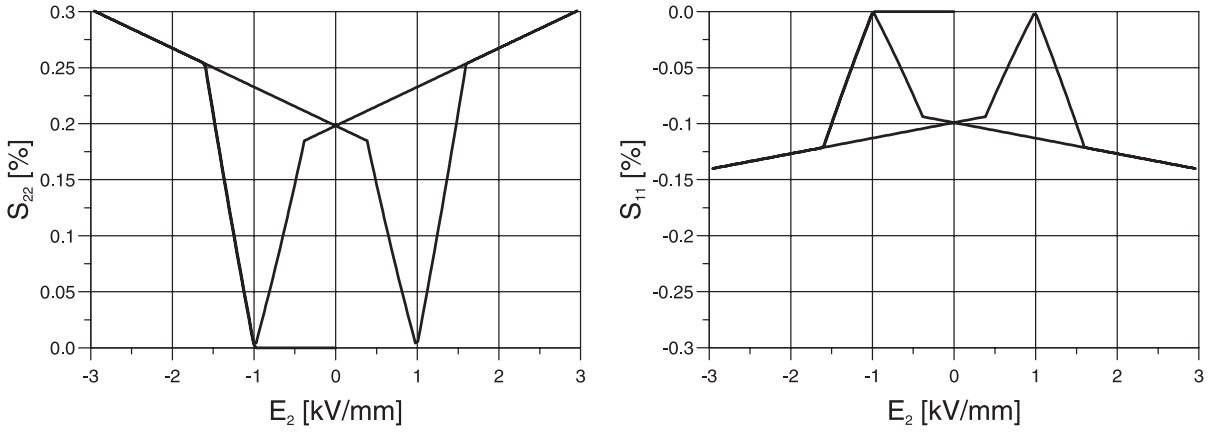

Fig. 5. Butterfly hysteresis in poling direction (left) and in direction perpendicular to poling (right).

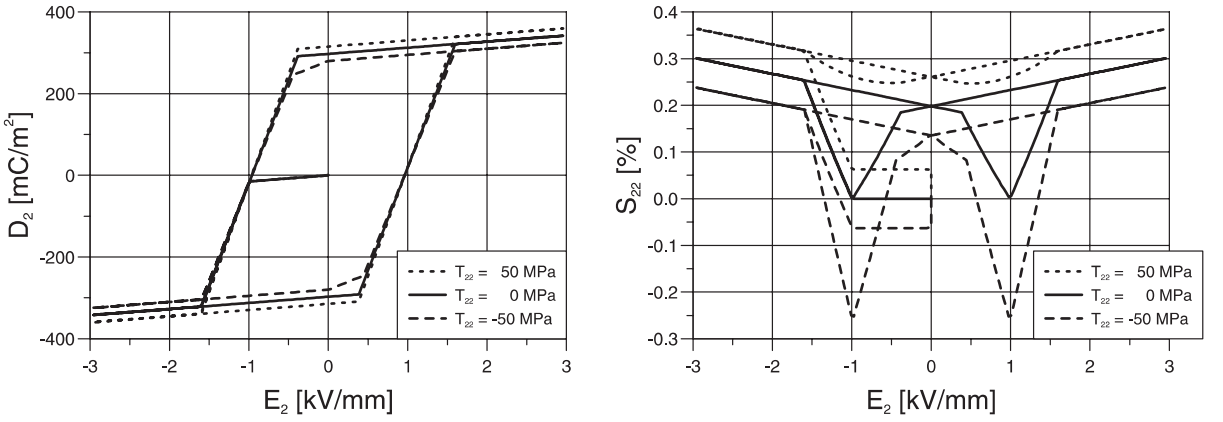

Fig. 6. Application of a constant mechanical stress followed by electric cycling – left: dielectric hystereses, right: butterfly hystereses.

In this context note that the magnitude of the superposed stress was chosen equal to the coercive stress σ_c. Thus, the effective value $\hat{\sigma}_c$ in Eq. (31) is even smaller after reversing of the electric field starts, for P_2^i and E_2 have opposite signs then, allowing for ferroelastic strain changes in this period. As a consequence, the amount of remanent strain S_{22}^p released during electric depolarization, is almost completely compensated by a mechanically induced ferroelastic remanent strain S_{22}^f which because of the tensile stress state, is positive, of course. According to Eq. (30), $\|\boldsymbol{S}^p\| + \left\|\boldsymbol{S}^f\right\| \leqslant \sqrt{3/2}S_{sat}$ has to hold, and the sum $S_{22}^i = S_{22}^p + S_{22}^f$ remains basicly on a constant level, i.e. S_{sat}.

In the case of a superposed compressive stress, represented by the dashed lines, we observe on the left-hand side of Fig. 6 likewise an additional contribution to the dielectric displacement in the fully poled range due to the direct piezoelectric effect, being negative this time. Also, it can be seen close to corners of the dielectric hysteresis, that reversing of the remanent polarization starts right after the electric field changes sign. This is due to the fact that the compressive stress reduces the effective value of $\hat{P}_{sat}$, Eq. (32), leading to early mechanical depolarization. The butterfly hysteresis on the right of Fig. 6 is affected significantly, again. Clearly, we see a superposed elastic compression strain which is constant. Once more, the difference to the other curves is most obvious during the period of electric depolarization. By the same mechanism as before, released remanent strain S_{22}^p is consumed by ferroelastic strain S_{22}^f, which is compressive this time. This is why S_{22}^i changes from $+S_{sat}$ to $-S_{sat}$ and the tips of the butterfly hysteresis are even below the initial elastic strain. These model properties compare at least qualitatively well to experimental findings of Lynch (1996).

In Fig. 7, the simulation of mechanical depolarization processes with varying values of a superposed electric field is shown. In each case, the horizontal line starting at the origin, represents initial poling by an electric field increased to 3.0 kV/mm. Then, the electric field is adjusted to a value held constant while a strong compressive stress is applied. Positive electric fields are oriented in the direction of initial poling and negative electric fields opposite to it. On the left-hand side of Fig. 7, we observe after a period of linear piezoelectric changing, a kink with subsequent rapid mechanical depolarization. Positive values of the electric field stabilize the existing remanent polarization against the compressive stress and lead to delayed onset of mechanical depolarization. On the other hand, a negative electric field, even if it is not strong enough to cause electric depolarization, leads to an early onset of mechanical depolarization. After depolarization is complete, meaning $\left\|\vec{\mathbf{P}}^i\right\| = P_\delta$, a second kink occurs. We recognize a remaining weak dependence of D_2 on T_{22} from the fact that the curves are not completely vertical, i.e. a fraction of the initial piezoelectricity has survived. On the right hand side of Fig. 7, we see the stress–strain behavior belonging to

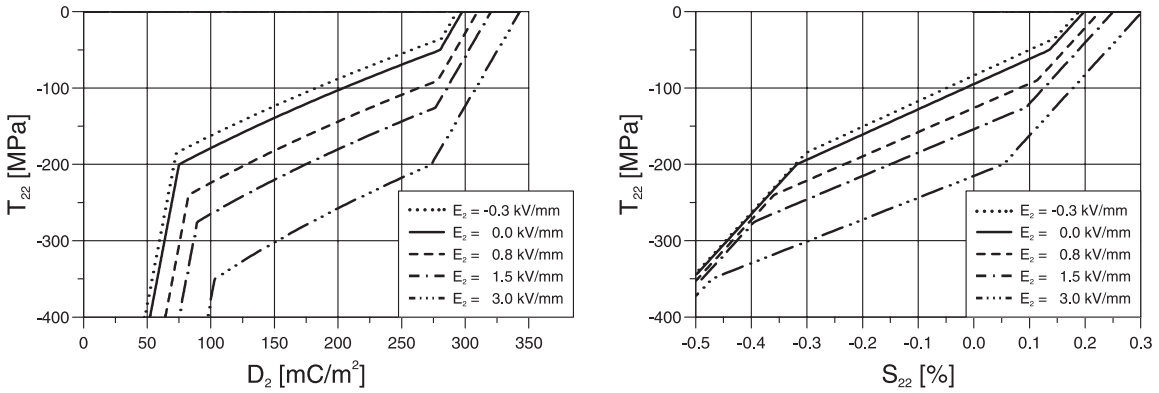

Fig. 7. Mechanical depolarization for different values of a superposed electric field. Positive electric fields are oriented in the direction of initial poling, negative electric fields opposite to it. Left: depolarizing stress over dielectric displacement and right: stress over strain.

the corresponding depolarization progress. Inelastic behavior starts at the same stress level as the respective depolarization. During the following period, the remanent strain S_{22}^{p} released as the remanent polarization is reduced, is replaced by compressive ferroelastic remanent strain S_{22}^{f}. When the reservoir for remanent strain is used up by ferroelastic strain, a second range of linear elastic behavior is reached.

4. Electro-mechanical analysis of a multilayer geometry

We now want to verify the benefits of our finite element tool by studying an example, simple on the one hand but typical of practical applications on the other. In this sense, we consider the structure shown in Fig. 8, having the principle design of a multilayer actuator. The geometry has been chosen in adaption to the literature. The dimensions L_1 and L_2 are assumed to be equal, as in the paper of Gong and Suo (1996). The numerical value for $L_1 = 205$ μm was taken from Hom and Shankar (1996). For the layer thickness $H = 57.5$ μm, half of the value of Hom and Shankar (1996) was used, in order to get a not too high ratio of the layer thickness to the lateral layer extension.

The boundary conditions applied and the finite element mesh can be seen in Fig. 9. Due to symmetry conditions, the upper electrode must not deform or rotate and is only allowed to translate parallel to its starting position. Concerning the strain state, the plane strain assumption has been employed. In order to simulate a poling process, the electric potential $V_{\text{appl}}(t)$ is prescribed as triangular loading history in the following manner: It first is increased from 0 to -170 V until $t_1 = 100$ s and then reduced to zero until

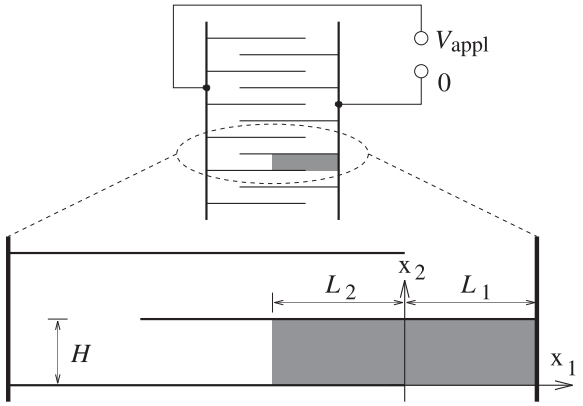

Fig. 8. Example structure for the verification of our finite element tool: $L_1 = L_2 = 205$ μm, $H = 57.5$ μm. Due to symmetry properties, only the shaded area is modeled.

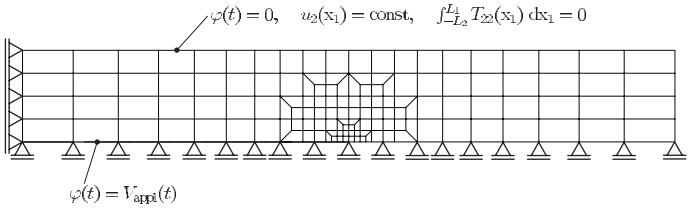

Fig. 9. Boundary conditions and finite element mesh for the electro-mechanical analysis of the structure shown in Fig. 8. The origin of the coordinate system is situated at the tip of the lower electrode with x_1 pointing to the right and x_2 to the top (see Fig. 8).

$t_2 = 200$ s. Thus, an electric field of approximately 3 kV/mm is reached in the region between the two electrodes, guaranteeing full poling. As we want to simulate a poling process without superposed mechanical load, the resultant force on the upper electrode has to vanish. Even though the mesh is refined towards the tip of the lower electrode, it still will be too coarse, to resolve the details of the fields in this region. But again, we want to point out that we rather want to demonstrate the basic benefits of our approach and do not yet have in mind to carry out detailed analyses on real structures.

4.1. Step 1: dielectric analysis

According to our two-step strategy presented in Section 3.1, we now consider the dielectric boundary problem first. From Fig. 10a and c, we see the electric potential at the instant $t = t_1 = 100$ s of the highest voltage and after unloading, i.e. $t = t_2 = 200$ s, respectively. No legends are shown as we only want to give a qualitative impression for the time being (for a quantitative result see Fig. 11). Borders between grey levels are lines of constant φ. In Fig. 10b, the vector field $\vec{\mathrm{P}}^{\mathrm{i}}_{\mathrm{diel}}$ of the purely dielectrically calculated remanent polarization is depicted.

At time $t = t_1$, we can distinguish three regions in Fig. 10a. First, the area next to the left border of the model is dominated by a constant gradient of the electric potential between the two electrodes. In the region next to the free right border, the electric potential is close to zero and no gradient is present. The middle region is characterized by the transition between the two homogeneous regions.

In Fig. 10b, this division in three regions is also revealed by the vector plot of the remanent polarization $\vec{\mathrm{P}}^{\mathrm{i}}_{\mathrm{diel}}$ calculated from the purely dielectric boundary value problem. The region on the left-hand side is fully poled, i.e. $\left\|\vec{\mathrm{P}}^{\mathrm{i}}_{\mathrm{diel}}\right\| = P_{\mathrm{sat}}$. It is connected to a completely unpoled region on the right by a transition area possessing an inhomogeneous $\vec{\mathrm{P}}^{\mathrm{i}}_{\mathrm{diel}}$ field.

Looking at the electric potential after unloading at $t = t_2$ in Fig. 10c, we clearly observe a non-vanishing distribution even though φ is zero at both electrodes. The reason for this, at first sight maybe surprising

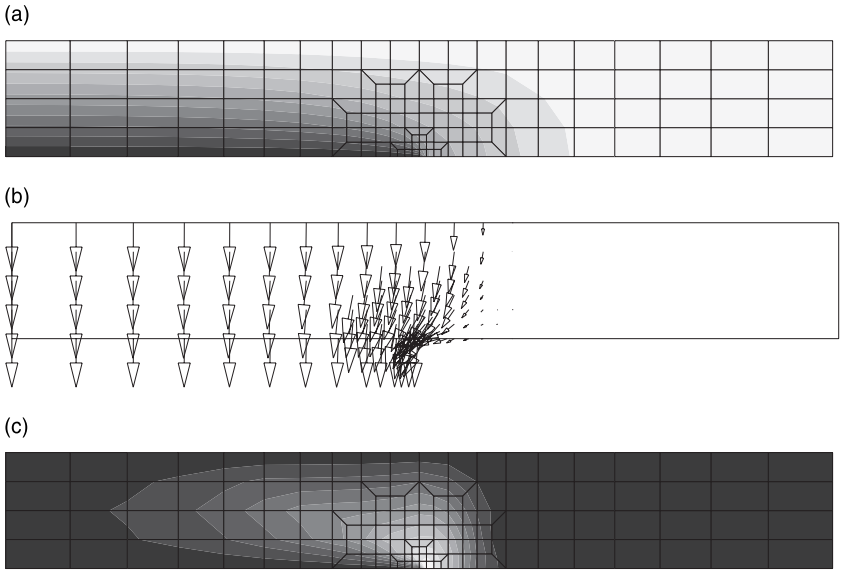

Fig. 10. (a) Electric potential φ at $t = t_1 = 100$ s ($V_{\mathrm{appl}} = -170$ V), (b) remanent polarization $\vec{\mathrm{P}}^{\mathrm{i}}_{\mathrm{diel}}$ at $t = t_2 = 200$ s. (c) electric potential φ at $t = t_2 = 200$ s ($V_{\mathrm{appl}} = 0$ V).

result, is given by a characteristic feature of our dielectric constitutive law. As can be seen in Fig. 10b, a non-zero remanent polarization distribution $\vec{P}^{i}_{diel}(\vec{x})$ remains after unloading. Now, taking into account the Gaussian law (43), the definition of the dielectric displacement (45), the additive decomposition (1), the constitutive equation (3), and the potential relation $\vec{E} = -\text{grad}\,\varphi$ for the electric field, we find the following Laplace equation for the electric potential at $t = t_2$:

$$\Delta\varphi = \frac{1}{\epsilon_0 + \epsilon}\,\text{div}\,\vec{P}^{i}_{diel}. \tag{46}$$

Thus, the divergence of the remanent polarization distribution acts as a volume charge density (in fact, this corresponds exactly to the macroscopic physical interpretaion of the polarization field, see e.g. Landau and Lifschitz (1967). Looking at Fig. 10b) again, we recognize that $\text{div}\,\vec{P}^{i}_{diel}$ may be non-zero in the neighborhood of the electrode tip, since $\vec{P}^{i}_{diel}(\vec{x})$ is inhomogenous there. As a matter of fact, it is exactly this region, where we find the non-vanishing values for the electric potential after unloading in Fig. 10c.

From Fig. 11, we can get an idea of the orders of magnitude of the electric potential. In this figure, the electric potential φ is plotted along the bottom border line of our model. First, represented by the dotted line, the linear dielectric solution for $t = t_1$ is shown as reference. Note that the linear dielectric constitutive law $\vec{P} = \epsilon\vec{E}$ is obtained from our model as a special case for $E_c \to \infty$. Along the electrode, $\varphi = -170$ V as required by the boundary conditions. Then, for $x_1 \geqslant 0$, φ decays until it reaches the value zero at the free end on the right hand side. The linear dielectric solution for $t = t_2$ is not plotted, since it simply vanishes identically. For $t = t_1$, the solution obtained with our ferroelectricity law is given by the solid curve. It is qualitatively similar to the linear dielectric solution; however, it decays more rapidly for $x_1 \geqslant 0$. A significant difference occurs for $t = t_2$, which can be seen from the dashed line. As required by the boundary condition, the ferroelectric solution vanishes along the electrode. Right behind the tip of the electrode at $x_1 = 0$, φ increases rapidly to values close to 30 V which is certainly not a neglectable order of magnitude compared to the values at the instant of highest voltage V_{appl}. With increasing distance from the tip, φ decreases again and finally is zero in the unpoled region. Since we consider a theory of a non-conducting dielectric with infinite resistivity, we obtain a non-vanishing distribution of the electric potential which will persist even without external voltage and cannot be balanced out by charge flow.

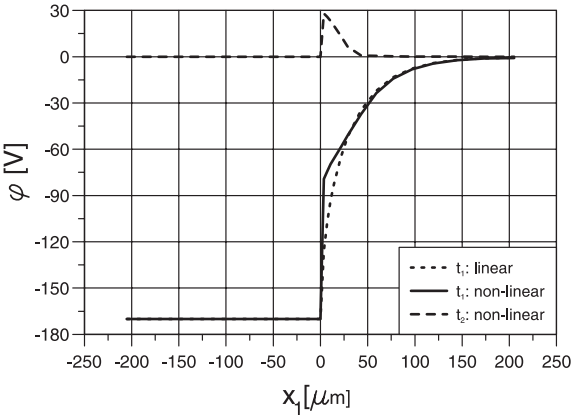

Fig. 11. Plot of the electric potential φ along the bottom border of the model: (- - -) $t = t_1$, linear dielectric solution, (—) $t = t_1$, ferroelectric solution and (– – –) $t = t_2$, ferroelectric solution.

4.2. Step 2: electro-mechanical stress analysis

As explained in Section 3.1, the mechanical boundary conditions for displacements and stresses enter the picture in step 2. Besides them, the history of the electric potential calculated in step 1 is prescribed at each node, thus representing the influence of the electric boundary conditions. However, this does not mean, that the derived electric quantities such as polarization will necessary be the same as in step 1. This is because the complete electro-mechanically coupled constitutive law is solved in step 2, and the polarization now also depends on mechanical quantities.

For a detailed discussion of the results, we will focus our attention on three characteristic locations in our model, i.e. the elements 126, 91, and 19 indicated in Figs. 12 and 13. Element 126 stands for the fully poled region, element 91 represents the electro-mechanically passive zone close to the free end and element 19 is situated near the "hot spot" at the electrode tip.

4.2.1. The fully poled region

From Fig. 10a, we can conclude that the electric field is oriented homogeneously in the vertical direction in the region between the two electrodes. Fig. 14 shows the corresponding components of the remanent polarization and the dielectric displacement, respectively, plotted over the the electric field in the direction of x_2. In the left figure, we see that poling starts, as $|E_2|$ reaches the coercive field E_c. Soon, P_2^{i} reaches the maximum remanent polarization $P_{\mathrm{sat}} = 0.3\ \mathrm{C/m^2}$ and remains constant as the field is increased further and during most of the unloading path. However, at $E_2 = -0.7$ kV/mm, we recognize a kink and subsequent reduction of $|P_2^{\mathrm{i}}|$. As we can conclude from the right plot of Fig. 16, compressive stresses above the coercive

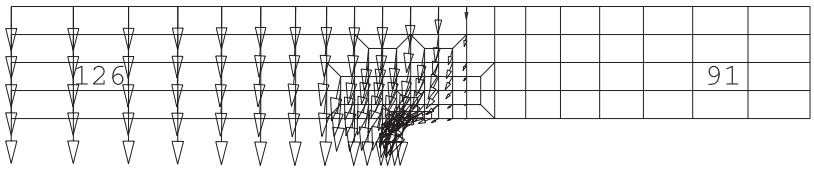

Fig. 12. Vector field of the remanent polarization $\vec{\mathrm{P}}^{\mathrm{i}}$ after unloading ($t = t_2$), calculated in the electro-mechanical step 2. See Fig. 13 for a zoom in the neighborhood of the tip of the lower electrode. The results for the labeled elements will be discussed in detail.

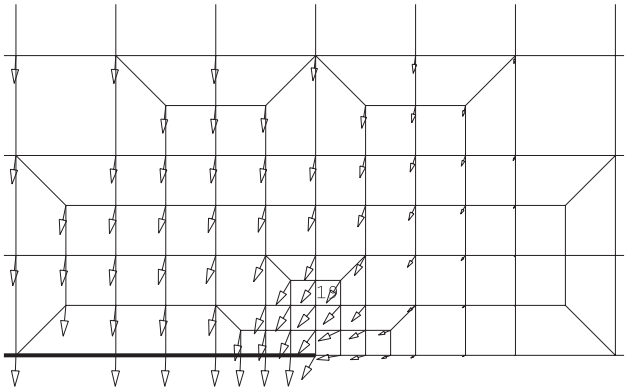

Fig. 13. Zoom in the neighborhood of the electrode tip showing the vector field of the remanent polarization $\vec{\mathrm{P}}^{\mathrm{i}}$ after unloading ($t = t_2$). Due to the extrapolation of results from the intergration points to the nodes, the numerical value of $\mathrm{P}_2^{\mathrm{i}}$ is not exactly zero in front of the tip.

stress develop during poling, the reason for which will be discussed later. These stresses lead to partial mechanical depolarization, and thus to the reduction observed as the electric field is removed. Note that such depolarization cannot be obtained in the first purely dielectric analysis of step 1, since no interaction between electric and mechanical fields is present then.

Looking at the right plot of the dielectric displacement D_2 in Fig. 14, we identify the onset of poling and saturation from the corresponding kinks as well. At first sight, it might be surprising that after saturation the magnitude of D_2, is smaller than $|P_2^{\mathrm{i}}|$. The reason for this is again the presence of a compressive stress state, which reduces the dielectric displacement by the direct piezoelectric effect with respect to the remanent polarization. This effect over-compensates the linear dielectric contribution to D_2 (see Eqs. (45), (1), and (3)).

In the left plot of Fig. 15, we see that the remanent deformation S_{22}^{p} representing the strain associated to the alignment of domains behaves just as the remanent polarization. During poling, a positive strain develops in the direction of poling, and is partly reduced as the mechanical depolarization takes place. The presence of a superposed compressive stress not only affects the remanent strain, rather we realize that the

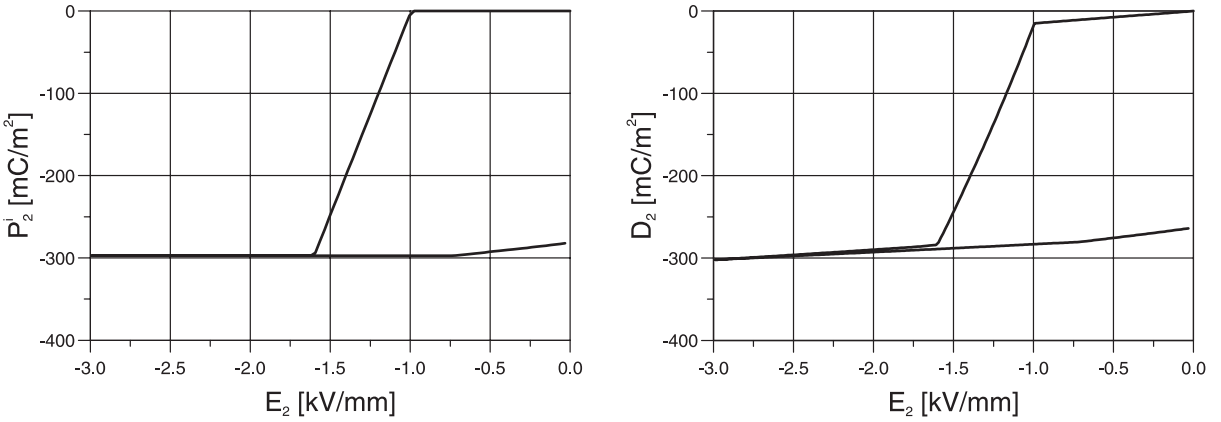

Fig. 14. Poling process in vertical direction: remanent polarization (left) and the dielectric displacement (right) over the electric field.

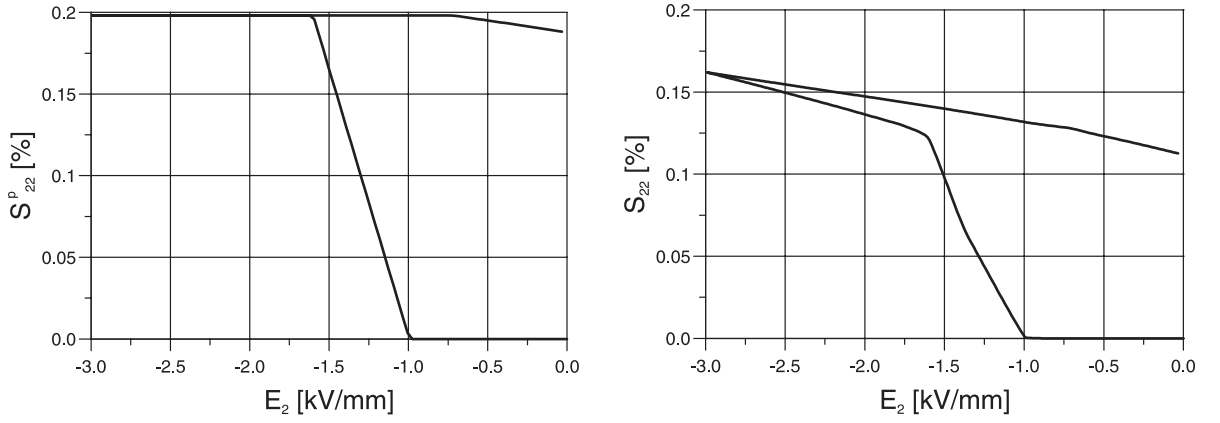

Fig. 15. Normal strains in poling direction over the electric field in poling direction – Left: remanent strains induced by poling and right: total strain.

total strain in poling direction is significantly smaller than its remanent part. This difference can be explained by a negative elastic strain belonging to the compressive stress.

From the left plot of Fig. 16, we observe that a significant compressive stress in poling direction is built up as the strain increases. It is caused by the passive region of the layer and will be explained later on. Since the stresses corresponding to the same strain values are lower during unloading, the related elastic strains are smaller as well. This difference of the elastic strains between loading and unloading leads to the opening observed in the right plot of Fig. 15 at the branch of the S_{22}–E_2 hysteresis belonging to saturated remanent strains. The S_{22}–E_2 curve shows a non-zero slope during unloading in contrast to the unpoled state. This is caused by the inverse piezoelectric effect induced by the poling process: In the poled state, there exists a linear coupling between the electric field and the deformation.

Fig. 17 shows the behavior in the directions perpendicular to poling. As can be expected, we see on the left hand side that the structure contracts in the x_1-direction during poling. Since the right border of our model is stress-free, almost no stresses are built up in the x_1-direction (not shown). Concerning the out-of-

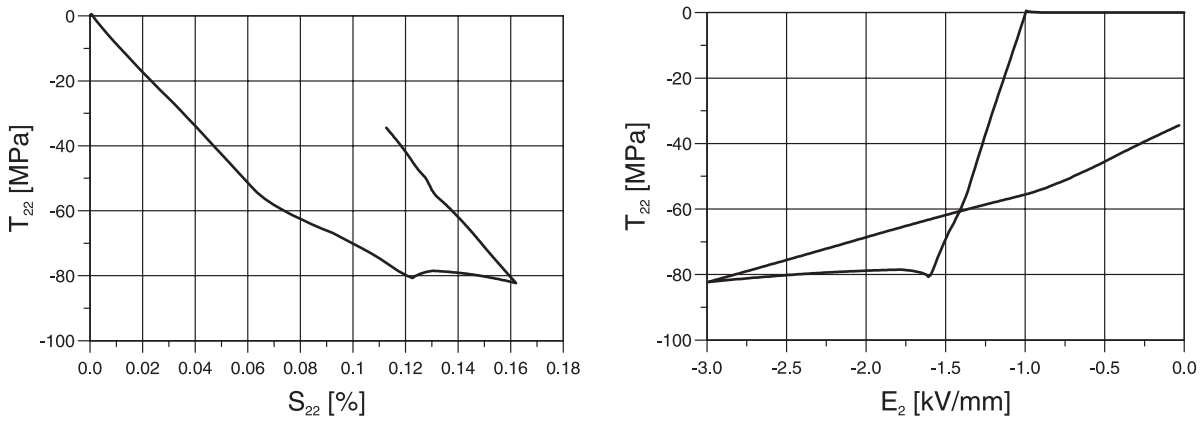

Fig. 16. Normal stress in the poling direction plotted over the corresponding strain component (left), and over the poling electric field (right).

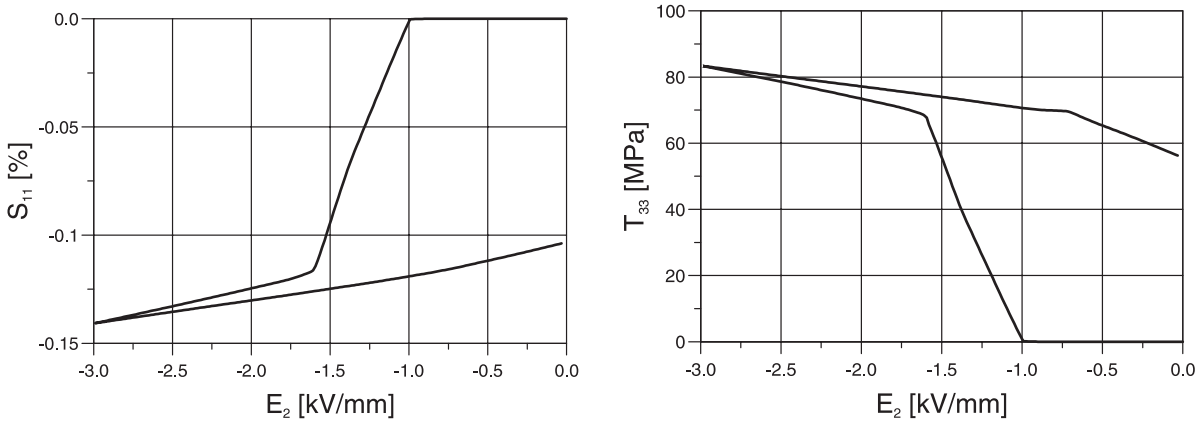

Fig. 17. Strains and stresses perpendicular to the poling direction – left: transverse strains in the x_1-direction and right: out-of-plane normal stresses.

plane-direction, the situation is just the other way around. Due to the plane strain assumption, no strains occur in the x_3-direction. This constraint causes severe tensile stresses in the out-of-plane direction, as the contraction due to poling occurring in both the x_1- and x_3-directions has to be compensated completely by tensile mechanical strains in the x_3-direction.

4.2.2. The electro-mechanically passive region

As Fig. 12 clearly shows, the region between the tip of the lower electrode and the free border on the right remains completely unpoled. From Figs. 10 and 11, we conclude that due to the configuration of the electrodes the electric potential stays in this region at low values even at the instant $t = t_1$ of highest voltage V_{appl}. In fact, in the left plot of Fig. 18 we see that at element 91 labeled in Fig. 12, the vertical electric field is orders of magnitude smaller than in the poled region. Because of this, we observe simply a linear dielectric response without hysteresis and remanent polarization. No electro-mechanical coupling is induced and this portion of the actuator remains electro-mechanically passive.

However, even though the electric loads are small, this does not mean that no hysteresis behavior occurs at all. Rather, we recognize in the right plot of Fig. 18 that ferroelastic processes occur, the reason for which will be discussed now. During poling, the region between the two electrodes elongates as a macroscopic polarization vector is built up. On the other hand, due to symmetry conditions, we have the constraint that the upper electrode must not deform or rotate. Only a translation parallel to its original position is allowed (see the beginning of Section 4, and Fig. 9). Because of this constraint, elongation of the poled region takes place exactly by the same amount as the passive region is forced to stretch. In the passive region, stresses are the only mechanism to cause deformation, and in fact, we clearly see in the right plot of Fig. 18 that tensile stresses are built up in the passive region as it is stretched by the poled zone. At the beginning, the stress response is elastic but eventually, the stresses reach a level sufficient for ferroelastic deformation, i.e. $\|\boldsymbol{T}^D\| = \sigma_c$. The increase of the stresses due to further stretching of the passive zone is now much more moderate. From the right plot of Fig. 15, we know that the strains S_{22} reach a peak value of approximately 0.16% at the instant $t = t_1$ of maximum voltage V_{appl} and are then reduced linearly during unloading. Due to the piezoelectricity induced by poling, the poled region becomes shorter as the external voltage is removed. By the constraint mentioned above, this reduction is also imposed on the passive region, leading to the elastic unloading process observed in the right plot of Fig. 18.

We now may return to the poled region for the time being and discuss the reason for the compressive stresses there. As we have just seen, tensile stresses are induced in the passive region as poling makes progress. However, we simulate a poling process without superposed mechanical load and thus the resultant

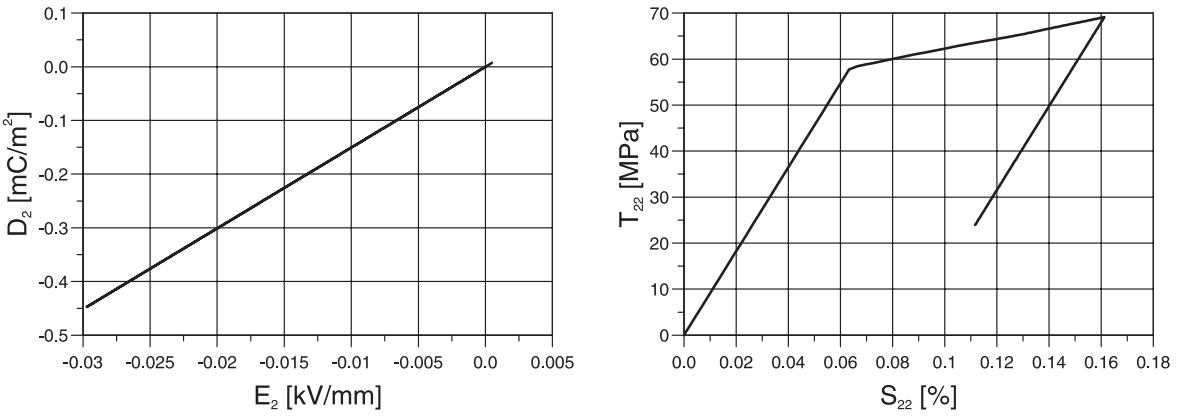

Fig. 18. Electro-mechanically passive region: dielectrically linear (left) but mechanically ferroelastic behavior (right).

force on the upper electrode was taken as zero. Therefore, the only way to maintain equilibrium is the development of compressive stresses in the poled region such that the resultant vertical forces in the poled and passive zones, respectively, cancel each other.

In view of these findings, we are in a position to discuss the right plot of Fig. 16. As soon as the coercive field is overcome, poling starts causing tensile stresses in the passive region. Thus the compressive stresses observed in Fig. 16 are induced by the mechanism explained above. As the remanent polarization saturates, the increase of the elongation of the poled region slows down and, consequently, so do the compressive stresses. As the electric field is removed, we have piezoelectric shortening of the poled region leading to elastic unloading of the passive zone. This in turn gives rise to the nearly linear reduction of the compressive stresses seen in Fig. 16.

4.2.3. The neighborhood of the electrode tip

The behavior in the poled and passive regions have more or less the character of uniaxial processes in the x_2-direction. From Figs. 12 and 13, it can be suspected that the processes near the electrode tip are of multiaxial nature and thus are quite difficult to interpret. This can clearly be confirmed by considering the left plot of Fig. 19, where the two components of the remanent polarization are plotted for element 19 (Fig. 13): The remanent polarization vector not only grows in magnitude, it also rotates during loading and unloading. At the beginning, $\vec{P}^i$ grows proportionally form point "O" to "A" with only minor changes of the direction. At point "A", the magnitude reaches its maximum value, i.e. $\left\|\vec{P}^i\right\| = P_{sat}$, and it cannot grow further. However, loading is continued and we observe from "A" to "B", rotation of the saturated remanent polarization state without increase of the magnitude (cf. Section 2.3 and Fig. 2). During unloading from "B" to "C", basically only the P_1^i-component is reduced, rotating $\vec{P}^i$ partly back to the direction of the initial loading path "O"–"A".

Probably the most important question for practical applications concerns the residual stress state after unloading induced by the poling process. In the right plot of Fig. 19, we see the normal stresses perpendicular to the electrodes plotted along the lower border of our model. As can be expected, stresses are stronger at the instant $t = t_1$ of maximum voltage, than they are after unloading ($t = t_2$). However, even after removing the external electric load, we observe a significant residual stress state. In the poled region, a compressive stress of approximately -35 MPa is present. More dangerous for the actuator, a tensile stress

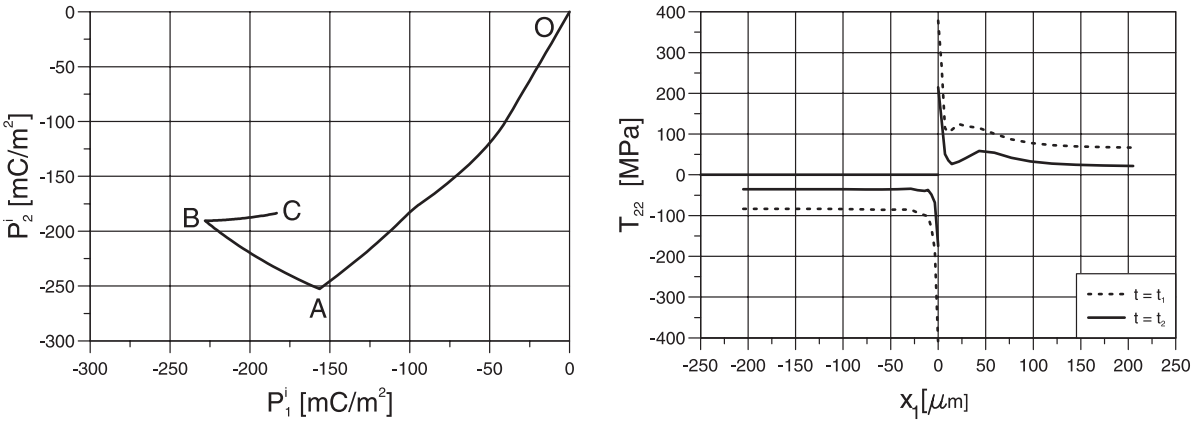

Fig. 19. Left: Development of the components of the remanent polarization during loading (O–A–B) and unloading (B–C). Right: Normal stresses perpendicular to the electrodes plotted along the lower border of the layer (the horizontal line represents the lower electrode) – (- - -): $t = t_1$, (—): $t = t_2$.

state of over 20 MPa is found in the passive region towards the free right border. This is exactly the region, where the so-called poling cracks are known to occur. In this context please note that the tensile strength of piezoceramics may be as low as the order of magnitude of these stresses induced by poling. Right in the neighborhood of the tip, we have severe stress intensifications. We find compressive stresses of up to -180 MPa approaching from the poled region and tensile stresses of over 200 MPa approaching the tip from the passive zone. However, our mesh is probably too coarse, to resolve the stress fields in full detail.

A comment has to made concerning the geometry considered here. In our example, we chose $L_2 = L_1$ while L_2 is much larger than L_1 in realistic geometries. For the passive region, the case $L_2 \gg L_1$ is even more dangerous. In this case, the compressive stresses in the poled region will be reduced as the given resultant tensile force in the passive region has to be balanced by a compressive force of equal magnitude resulting from a much larger region. Because of being too small to oppose any constraint on the poled region, the passive region will then be forced to stretch by nearly the full remanent poling strain. As a consequence, the higher tensile strains will lead to higher tensile stresses. In any case, there will be stress peaks near the tip of the electrode.

5. Conclusion

A simple phenomenological model for the ferroelectric and ferroelastic properties of piezoceramics has been given in a three-dimensional tensorial formulation. The model has been implemented in the non-linear finite element code PSU. The electro-mechanical analysis is carried out in a two-step scheme known from thermomechanics: The electric potential calculated in the first dielectric step is prescribed in the second step, where the stresses are analyzed.

As a demonstration example, the finite element tool is applied to a multilayer-like structure. It turns out that the response of the structure is dominated by the presence of ferroelectric and ferroelastic large signal hysteresis effects. The divergence of the remanent polarization field leads to a non-zero electric potential field even after removing the poling voltage at the electrodes. More importantly, a significant tensile stress state remains after poling in the passive region between the electrode tip and the free border of the actuator. Even if, after poling, the actuator is operated in the small signal regime with small stress changes, the fact that they are superposed on the residual stress state will increase the danger of accelerated fatigue. Because of this, multilayer actuators are usually run under a superposed compressive load to avoid tensile stresses. In our example, this compressive load should be approximately -20 MPa. Such a compressive load may lead to mechanical depolarization with the consequence of reduced performance, even if we consider a realistic geometry with the poled region being much larger than the passive one ($L_2 \gg L_1$).

The finite element tool present here needs further improvement with respect to several aspects. Meanwhile, the fully coupled solution of the electro-mechanical problem has been realized (Kamlah and Böhle, 2000). The saturation criterion for the remanent strains can be refined in the sense that the different saturation levels for compressive and tensile deformation states are distinguished (cf. Fett et al., 1998). Furthermore, the dielectricity tensor ϵ and the elasticty tensor $\mathbb{C}$ can be formulated by transversally isotropic representations with the remanent polarization as the axis of anisotropy. Nevertheless, we consider our finite element tool as appropriate for analysing the influence of ferroelectric and ferroelastic hysteresis effects on piezoceramic devices. In particular, the effect of variations of geometry and material parameters can be studied.

Acknowledgements

The support by the Deutsche Forschungsgemeinschaft is gratefully acknowledged.

References

Bassiouny, E., Ghaleb, A.F., Maugin, G.A., 1988. Thermomechanical formulation for coupled electromechanical hysteresis effects – I. Basic equations, II. Poling of ceramics. Int. J. Engng. Sci. 26, 1279–1306.

Bassiouny, E., Maugin, G.A., 1989. Thermomechanical formulation for coupled electromechanical hysteresis effects – III. Parameter identification, IV. Combined electromechanical loading. Int. J. Engng. Sci. 27, 975–1000.

Balke, H., Drescher, J., Kemmer, G., 1998. Investigation of mechanical strain energy release rate as a fracture criterion for piezoelectric ceramics. Int. J. Fracture 89, 59–64.

Böhle, U., 1999. Phänomenologische Modellierung und Finite-Elemente-Simulationen von nichtlinearen elektromechanischen Vorgängen in ferroelektrischen Materialien. Wissenschaftliche Berichte, vol. FZKA 6247, Forschungszentrum Karlsruhe, Karlsruhe.

Allik, H., Hughes, T.J.R., 1970. Finite element method for piezoelectric vibration. Int. J. Num. Meth. Engng. 2, 151–157.

Bowen, L.J., Shrout, T., Schulze, W.A., Biggers, J.W., 1980. Piezoelectric properties of internally electroded PZT multilayers. Ferroelectrics 27, 42–48.

Cao, H., Evans, A.G., 1993. Nonlinear deformation of ferroelectric ceramics. J. Am. Ceram. Soc. 76, 890–896.

Chen, P.J., 1980. Three dimensional dynamic electromechanical constitutive relations for ferroelectric materials. Int. J. Solids Struct. 16, 1059–1067.

Chen, X., Fang, D.N., Hwang, K.C., 1997. Micromechanics simulation of ferroelectric polarization switching. Acta Mater. 45, 3181–3189.

Chen, W., Lynch, C.S., 1998. A micro-electro-mechanical model for polarization switching of ferroelectric materials. Acta Mater. 46, 5303–5311.

Chen, W., Lynch, C.S., 1999. Finite element analysis of cracks in ferroelectric ceramic materials. Engng. Fract. Mech. 64, 539–562.

Chen, P.J., Marsden, M.M. 1981. One dimensional polar responses of the electrooptic ceramic PLZT 7/65/35 due to domain switching. Acta Mech. 41, 255–264.

Chen, P.J., Montgomery, S.T., 1980. A macroscopic theory for the existence of the hysteresis and butterfly loops in ferroelectricity. Ferroelectrics 23, 199–208.

Chen, P.J., Peercy, P.S., 1979. One dimensional dynamic electromechanical constitutive relations of ferroelectric materials. Acta Mech. 31, 231–241.

Cross, L.E., 1993. Ferroelectric ceramics: tailoring properties for specific applications. In: Setter, N., Colla, E.L. (Eds.), Ferroelectric Ceramics: Tutorial Reviews, Theory, Processing, and Applications. Birkhäuser, Basel, pp. 1–86.

Cross, L.E., 1995. Ferroelectric materials for electromechanical transducer aplications. Jpn. J. Appl. Phys. 34, 2525–2532.

Cross, L.E., 1998. Recent developments in piezoelectric ferroelectric materials and composites. In: Tomlinson, G.R., Bullough, W.A. (Eds.), Proceedings of the Fourth European Conference on Smart Structures and Materials. IOP Publishing, pp. 89–97.

Dafalias, Y.F., Popov, E.P., 1976. Plastic internal variables formalism of cyclic plasticity. J. Appl. Mech. 43, 645–651.

Dunn, M., 1994. The effect of crack face boundary conditions on the fracture mechanics of piezoelectric solids. Engng. Fract. Mech. 48, 25–39.

Fan, J., Stoll, W.A., Lynch, C.S., 1999. Nonlinear constitutive behavior of soft and hard PZT: experiments and modeling. Acta Mater. 47, 4415–4425.

Fatuzzo, E., Merz, W.J., 1967. Ferroelectricity. North-Holland, Amsterdam..

Feldtkeller, E., 1973. Dielektrische und magnetische Materialeigenschaften, vols. I and II, Bibliographisches Institut, Mannhein et al.

Fett, Th., Munz, D., Thun, G., 1998. Nonsymmetric deformation behavior of lead zirconate titanate determined in bending tests. J. Am. Ceram. Soc. 81, 269–272.

Gaudenzi, P., Bathe, K.-J., 1995. An iterative finite element procedure for the analysis of piezoelectric continua. J. Intelligent Mater. Syst. Struct. 6, 266–273.

Ghandi, K., Hagood, N.W., 1997. A hybrid finite element model for phase transition in nonlinear electro-mechanically coupled material. In: Varadan, V.V., Chandra, J. (Eds.), Smart Structures and Materials 1997: Mathematics and Control in Smart Structure. Proceedings of SPIE, vol. 3039, pp. 121–140.

Gong, X., 1995. Stresses near the end of an internal electrode in multilayer electrostrictive ceramic actuators. Mat. Res. Soc. Symp. Proc. 360, 83–88.

Gong, X., Suo, Z., 1996. Reliability of ceramic multilayer actuators: a nonlinear finite element simulation. J. Mech. Phys. Solids 44, 751–769.

Hom, C.L., Shankar, N., 1994. A fully coupled constitutive model for electrostrictive ceramic materials. J. Intelligent Mater. Syst. Struct. 5, 795–801.

Hom, C.L., Shankar, N., 1995. A numerical analysis of relaxor ferroelectric multilayered actuators and 2-2 composite arrays. Smart Mater. Struct. 4, 305–317.

Hom, C.L., Shankar, N., 1996. A finite element method for electrostrictive ceramic devices. Int. J. Solids Struct. 33, 1757–1779.

Huber, J.E., Fleck, N.A., Landis, C.M., McMeeking, R.M., 1998. Constitutive model of ferroelectrics. J. Mech. Phys. Solids 47, 1663–1697.

Huo, Y., Jiang, Q., 1997. Modeling of domain switching in polycrystalline ferroelektric ceramics. Smart Mater. Struct. 6, 441–447.

Hutter, K., van de Ven, A.A.F., 1978. Field matter interactions in thermoelastic solids. In: Ehlers, J., Hepp, K., Kippenhahn, R., Weidenmüller, H.A., Zittartz, J. Lecture Notes In Physics, vol. 88. Springer, Berlin.

Hwang, S.C., Lynch, C.S., McMeeking, R.M., 1995. Ferroelectric/ ferroelastic interactions and a polarization switching model. Acta Metall. Mater. 43, 2073–2084.

Hwang, S.C., McMeeking, R.M., 1998. A finite element model of ferroelectric polycrystals. Ferroelectrics 211, 177–194.

Hwang, S.C., McMeeking, R.M., 1999. A finite element model of ferroelastic polycrystals. Int. J. Solids Struct. 36, 1541–1556.

Jaffe, B., Cook, W.R., Jaffe, H., 1971. Piezoelectric Ceramics. Academic Press, London.

Kamlah, M., Böhle, U., 2000. On a non-linear finite element method for piezoelectric structures made of hysteretic ferroelectric ceramics. In: Lynch, Ch.S. (Ed.), Smart Structures and Materials 2000. Active Materials: Behavior and Mechanics. Proceedings of SPIE, vol. 3992.

Kamlah, M., Böhle, U., Munz, D., Tsakmakis, Ch., 1997. Macroscopic description of the non-linear electro-mechanical coupling in ferroelectrics. In: Varadan, V.V., Chandra, J. (Eds.), Smart Structures and Materials 1997: Mathematics and Control in Smart Structures. Proceedings of SPIE, vol. 3039, pp. 144–155.

Kamlah, M., Böhle, U., Munz, D., Tsakmakis, C., 1998. Macroscopic modeling of the non-linear electro-mechanical coupling in ferroelectrics. In: In: Gabbert., U. (Ed.), Modelling and Control of Adaptive Mechanical Structures. Proceedings of the EUROMECH 373 Colloquium, Fortschritt-Berichte VDI, Series 11, vol. 268. Düsseldorf, pp. 53–62.

Kamlah, M., Tsakmakis, C., 1999. Phenomenological modeling of the non-linear electro-mechanical coupling in ferroelectrics. Int. J. Solids Struct. 36, 669–695.

Kumar, S., Singh, R.N., 1996. Crack propagation in piezoelectric materials under combined mechanical and electrical loadings. Acta Mater. 44, 173–200.

Kuna, M., 1998. Finite element analyses of crack problems in piezoelectric structures. Comp. Mater. Sci. 13, 67–80.

Landau, L.D., Lifschitz, E.M., 1967. Elektrodynamik der Kontinua, Akademie Verlag, Berlin.

Lange, K. (Ed.), 1993. PSU: Prozeßsimulation in der Umformtechnik. Springer, Berlin.

Lines, M.E., Glass, A.M., 1977. Principles and Applications of Ferroelectrics and Related Materials. Clarendon Press, Oxford.

Lübbing, Ch., Keck P., Hessenberger, K., Herrmann, M., 1994. Das PSU-Programmsystem - aktueller Stand und Anwendungen. Numerische und experimentelle Methoden in der Statik und Dynamik, Institut für Statik und Dynamik der Luft- und Raumfahrtkonstruktionen, Stuttgart University.

Lübbing, Ch., 1997. Zur Stabilität von gestaffelten Finite-Elemente Berechnungen. Berichte aus dem Institut für Statik und Dynamik der Luft- und Raumfahrtkonstruktionen, vol. 18–97. Dissertation thesis, Stuttgart University.

Lynch, C.S., 1996. The effect of uniaxial stress on the electro-mechanical response of 8/65/35 PLZT. Acta mater. 44, 4137–4148.

Lynch, C.S., 1998.On the development of multiaxial phenomenological constitutive laws for ferroelectric ceramics. J. Intelligent Mater. Syst. Struct. 9, 555–563.

Maugin, G.A., 1988. Continuum Mechanics of Electromagnetic Solids. Elsevier, Amsterdam.

Maugin, G.A., Pouget, J., Drouot, R., Collet, B., 1992. Nonlinear Electromechanical Couplings. Wiley, Chichester.

McMeeking, R.M.,1989. Electrostrictive stresses near crack-like flaws. ZAMP 40, 615–627.

Michelitsch, Th., Kreher, W., 1998. A simple model for the nonlinear material behavior of ferroelectrics. Acta Mater. 46, 5085–5094.

Newnham, R E, 1989. Electroceramics Rep. Prog. Phys. 52, 123–156.

Pak, Y.E., 1992. Linear electro-elastic fracture mechanics of piezoelectric materials. Int. J. Fracture 54, 79–100.

Parton, V.Z., Kudryavtsev, B.A., 1988. Electromagnetoelasticity. Piezoelectrics and Electrically Conductive Solids. Gordon and Breach, New York.

Schäufele, A., Härdtl, K.H., 1996. Ferroelastic properties of lead zirconate titanate ceramics. J. Am. Ceram. Soc. 79, 2637–2640.

Simo, J.C., 1988. A framework for finite strain elastoplasticity based on maximum dissipation and the multiplicative decomposition: part I. continuum formulation. Comp. Meth. Appl. Mech. Engng. 66, 199–219.

Sosa, H., 1992. On the fracture mechanics od piezoelectric solids. Int. J. Solids Struct. 29, 2613–2622.

Steinkopff, Th., 1999. Finite-element modelling of ferroic domain switching in piezoelectric ceramics. J. Eur. Ceram. Soc. 19, 1247–1249.

Suo, Z., 1991. Mechanics concepts for failure in ferroelectric ceramics. In: Srinivasan, A.V. (Ed.), Smart Structures and Materials AD-vol. 24. AMD-Vol. 123, ASME, New York, pp. 1–6.

Suo, Z., Kuo, C.-M., Barnett, D.M., Willis, J.R., 1992. Fracture mechanics for piezoelectric ceramics. J. Mech. Phys. Solids 40, 739–765.

Uchino, K., 1993. Ceramic actuators: principles and applications. MRS Bulletin, April issue, pp. 42–48.

Yang, W., Suo, Z., 1994. Cracking in ceramic actuators caused by electrostriction. J. Mech. Phys. Solids 42, 649–663.